EXPERIMENTAL DETERMINATION OF THE FLOW FIELD VELOCITY AND STRAIN RATE IN A LAMINAR OPPOSED FLOW H_2/AIR DIFFUSION FLAME, VIA LASER DOPPLER ANEMOMETRY

by

Siew-Hock Yeo

Thesis submitted to the Faculty of the
Virginia Polytechnic Institute and State University
in partial fulfillment of the requirements for the degree of

MASTER OF SCIENCE

in

Mechanical Engineering

APPROVED:

Clinton L. Dancey
Clinton L. Dancey, Chairman

Richard J. Roby
Richard J. Roby

Larry Roe
Larry A. Roe

December 1990
Blacksburg, Virginia

EXPERIMENTAL DETERMINATION OF THE FLOW FIELD VELOCITY AND STRAIN RATE IN A LAMINAR OPPOSED FLOW H_2/AIR DIFFUSION FLAME, VIA LASER DOPPLER ANEMOMETRY

by

Siew-Hock Yeo
Dr Clinton L.Dancey, Committee Chairman
Mechanical Engineering

(ABSTRACT)

An experimental investigation of an opposed flow hydrogen-air diffusion flame was conducted. The purpose was to experimentally determine the flow field velocity and corresponding strain rate under different operating flow conditions. An axisymmetric opposed jet burner was employed in this experiment where air was supplied to one circular tube, while fuel and diluent were supplied to the opposing circular tube. Velocity measurements were made under two different operating flow rates, via the laser Doppler anemometer. The experimental results are used to assess current counterflow diffusion flame modeling approximations.

The data shows that the radial velocity is approximately linear with radial coordinate, as assumed by most modelings. The boundary conditions (uniform axial velocity, and linear radial velocity) assumed by the potential flow model are appropriate at a particular location upstream of the boundary layer region; and the supply air strain rate approximates the potential flow strain rate, going into the flame boundary layer region. Qualitatively, the plug flow model is a better approximation to the velocity distribution for both flow cases.

ACKNOWLEDGEMENTS

Many thanks are due to Dr. Clinton L. Dancey, my thesis advisor. His guidance and thoughts made my introduction to graduate study and research interesting and rewarding. Also, I would like to take this opportunity to thank Dr. Richard J. Roby and Dr. Larry A. Roe for serving as the committee members in this work. I would like to thank Dr. Roby for his kind consent for the use of his computer facility for preparing this thesis.

Among the many friends that have helped me along the way, I would like to especially thank Mr. J.A. Wang for his help and patience in teaching me the LDA system and the seeder operations.

Finally, I would like to acknowledge the support of Dr. G. Pellett's office of NASA-Langley Research Center, without which, this thesis would not be possible.

TABLE OF CONTENTS

APPENDIX

LIST OF FIGURES

LIST OF TABLES

1. INTRODUCTION

Most reacting flows of practical interest are turbulent in nature (gas turbine combustors, rocket engines, oil furnaces, etc). Characteristics of turbulence include: stretching and straining motion which is random in time and space; steepening of temperature and concentration gradients, which enhance mass and energy transfer rates; among others. As such, the transport properties of turbulent flames (effective mass diffusivity, thermal conductivity, etc) are functions of the flow rather than the fluid.[1] The laminar flamelet concept, in the studies of turbulent flames, views a turbulent diffusion flame as an ensemble of strained laminar diffusion flamelets.[2-19] Of fundamental interest in the studies of turbulent flames are the local flame extinction limits and pollutant formation. The counterflow geometry diffusion flame is the most representative steady flow field for the study of chemistry models and transport effects in laminar diffusion flamelets.[3,4] Successful prediction of extinction and species formation in such flames demands a detailed understanding of the fluid mechanical processes (strain rate and velocity fields) in such flow fields as these processes affect the transport of significant thermodynamic properties.[2]

In diffusion flames, the chemical reaction rate is often much faster than the diffusion rate of species into the flame zone. However, in cases where the mass flow rates of fuel and oxidizer are much higher,for example, in the case of strained laminar flamelets, the chemical reaction rate can be of the same order of magnitude as the diffusion rate; and in limiting cases, the chemical reaction could abruptly cease. Such an event is termed "convection extinction" by Spalding,[20] and "strain induced extinction" by Pellet.[5,6]

Two types of counterflow geometry have been used experimentally in the studies of laminar diffusion flame extinction limits: a counterflow diffusion flame between two opposed gaseous jets (circular or matrix jets); and a diffusion flame established in the forward stagnation region of a porous burner suspended in a uniform oxidizer flow (porous sphere or porous cylinder).[12] However, current numerical models of counterflow geometry diffusion flames have been less than satisfactory in predicting experimental extinction limits, reported so far, in these burner geometries.[19] This calls into question the assumptions and approximations used in those models.

The purpose of the present work is to experimentally assess some of the assumptions and approximations made in published counterflow diffusion flame numerical models,[13-17] and to provide a data set to aid in model development. One major difficulty encountered in validating numerical methods has been the absence of detailed experimental data on the velocity field in such straining reacting flows. Most existing experimental data[5,9-12] of the velocity field in CFDF's includes only of the axial velocity component on the centerline of the burner. Flow field velocity measurements will provide vital data necessary for development of improved strained H_2/Air diffusion flame models.

A laminar CFDF was used in the present experimental study of a hydrogen-air diffusion flame in a straining flow field. Figure 1 is a schematic illustration of a typical CFDF stabilized by two steady, laminar, axisymmetric counterflowing jets, that is used by

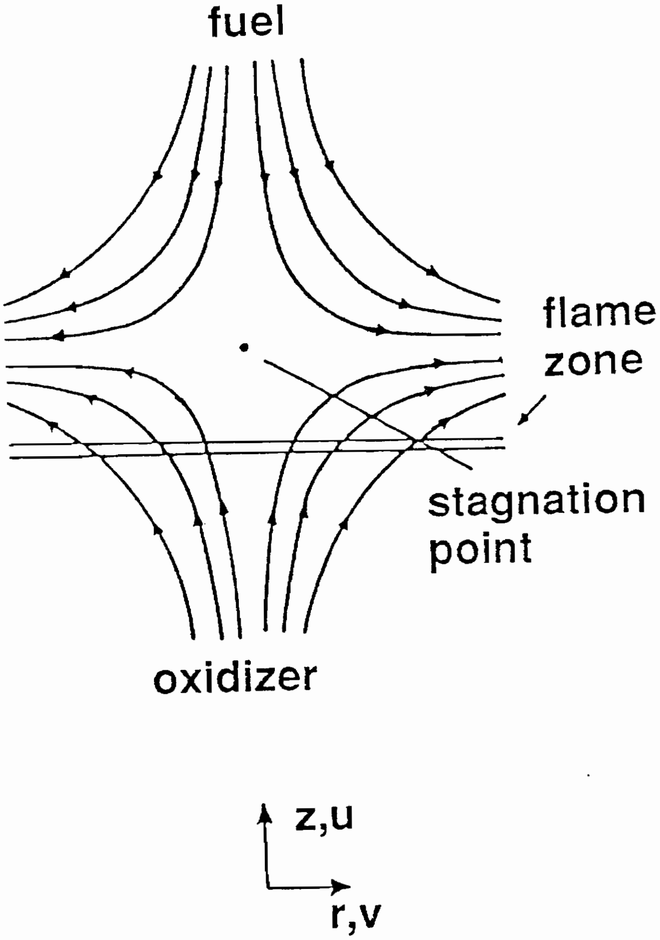

Figure 1 A schematic illustration of a typical CFDF

many investigators in the study of laminar diffusion flames. This was achieved using an opposed jet burner (OJB) arrangement previously developed at NASA-LaRC. Figure 2 is a photograph of the OJB without the enclosure box, showing the tubes and their holder. This OJB arrangement employed two long opposing circular tubes of 7 mm diameter (D) in a vertical orientation, with a tube separation of approximately 10 mm. The air flow (lower tube) was seeded with micron-size chemically stable refractory particles; while the fuel flow (upper tube) was unseeded and cooled by a water jacket. The fuel tube holder was also cooled continuously.

Velocity measurements on the air side of the CFDF flow field were made using a two-color, dual-beam, laser Doppler anemometer (LDA) technique, an optical, non-intrusive technique. Measurements included both the axial and radial velocity components through out the air side flow field under several burner operating fuel, diluent, and air flow rates. The flow field velocity structure and the strain rates were determined from these experimental velocity measurements.

1.1 Background and Literature Reviews

1.1.1 Counterflow diffusion flame

In diffusion flames, the characteristic chemical reaction time (τ_c) is frequently much

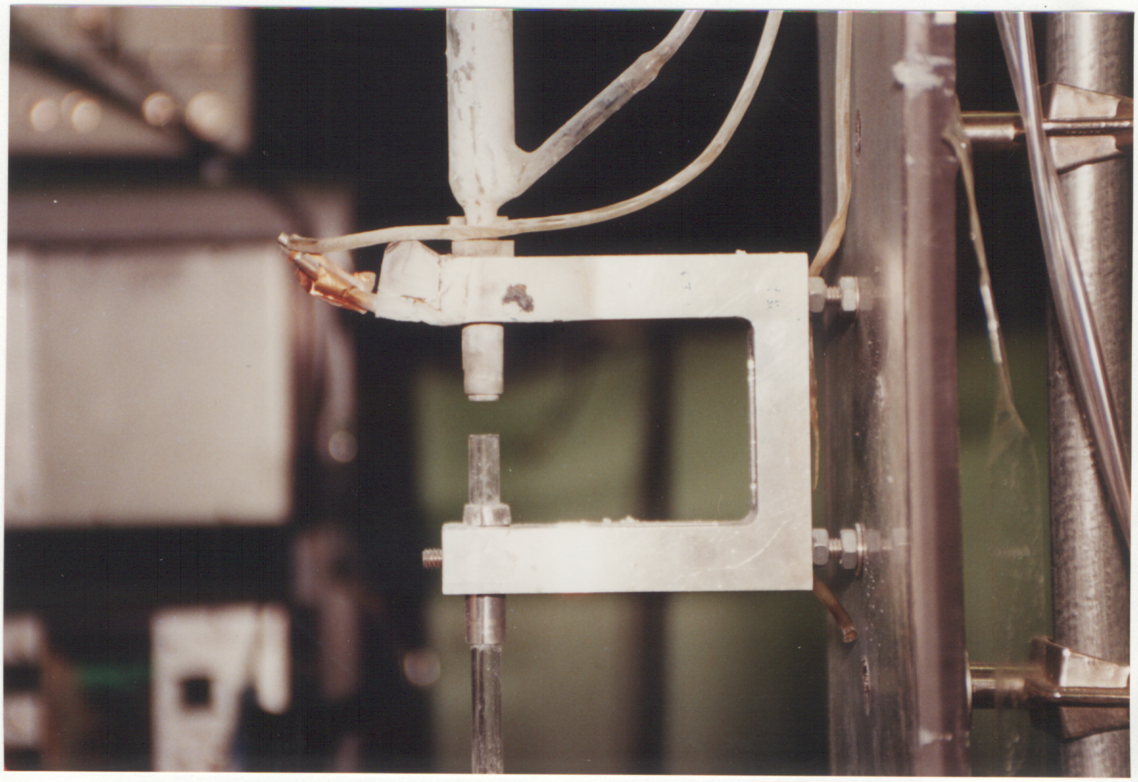

Figure 2 A close-up photograph of the OJB showing both the upper and lower tubes with the tube holder and the tube sleeves

smaller than the characteristic diffusion time (τ_d) of species into the reaction zone. Consequently, the chemical reaction occurs in a very narrow zone or flame sheet. Therefore, the whole combustion process is said to be controlled by the diffusion rates of the fuel and oxidizer into this flame sheet.[10]

The first successful quantitative analysis of the diffusion flame using the Flame Sheet Model was published by Burke and Schumann in 1928,[21] where it was assumed that the fuel and oxidizer were in stoichiometric proportions at the flame sheet surface.[1] In this work, Burke and Schumann were able to accurately predict the shape and height of a coaxial cylindrical diffusion flame. However, such a flame sheet model is unable to predict the observed phenomenon of flame blow-out, which occurs in a CFDF when the flow rates of both the fuel and oxidizer are increased sufficiently.[12]

In CFDF's, a critical flow velocity can be reached where the chemical reaction rate can not "keep up" with the reactant supply. Consequently, the chemical reaction can cease abruptly. This is termed flame extinction and is the result of the chemical limitations of the reaction. This critical flow velocity can be thought to represent the measure of the chemical limitations, or the overall maximum reaction rates, in the flame zone.[8]

Theoretical studies of these chemical limitations by Spalding[20] were prompted by his observation of the extinction of diffusion flames by forced convection around burning drops. This led to a pioneering experimental investigation of "strain induced extinction" by Potter et al,[8] using two circular opposing jet tubes. Potter showed that this setup was suitable for determining such chemical limitations of a diffusion flame, expressed as Apparent Flame Strength (AFS). The Apparent Flame Strength, as defined by Potter, is the average of fuel and oxidizer mass fluxes at flame extinction. Potter found that the AFS was independent of the tube separation over a range of 0.4D to 4D, when the jet flows exhibited a fully developed laminar parabolic exit velocity profile. The AFS was also found to be linearly proportional to the diameter (D) of the tube used. The investigation found that for uniform velocity profiles at the jet exits, various tube separations have an effect on the measured AFS. Also, Potter et al. suggested that the local velocities within the flow field, rather than the averaged jet exit velocity, determined the actual strain rate at flame extinction. This will be discussed further later in this thesis. Finally, Potter confirmed that a H_2/air diffusion flame is present on the air side of stagnation as predicted by the Spalding theory.[22]

This pioneering study of laminar CFDF using opposed circular jets was followed by many experimental and analytical investigations. Experimentally, most investigations have avoided using the opposed circular jets geometry. Pandya and Weinberg[15] used a flat velocity profile in their measurements of temperature distribution and gas composition. Temperature, composition and flow pattern measurements using a porous cylinder (Tsuji burner, which is a 2-D planar flow rather than axisymmetric flow) were performed by Tsuji and Yamaoka.[9-12] In 1982 Tsuji published an extensive review of CFDF[12] where the porous cylinder burner results were emphasized.

The OJB technique introduced by Potter et. al. in 1962, was advanced and employed by Pellet et al.[5-7] at NASA-LaRC since 1986. This technique provided a means to study the various effects of facility-related air contaminants on the combustion and extinction properties of highly stretched H_2-air CFDFs.[5-7] Early experimental studies of air contaminant problems using shock tube ignition, jet stirred combustor residence time calculations, laminar burning velocity measurements, and ignition and combustion limits have been performed on hydrogen premixed flames, but relatively little has been reported on non-premixed H_2/air CFDFs.[5] Thus experimental studies were undertaken in the hope that increased knowledge of the hydrogen combustion processes (chemical kinetics and fluid mechanics), will lead to an improved understanding of the combustion of hydrogen with/ without contaminants. With this OJB arrangement, Pellett was able to observe the phenomena of "strain-induced" extinction with a CCD video camera. Also he discovered a previously unreported phenomena of flame restoration. With limited velocity measurements along the stagnation streamline, Pellett et al.[5,6] were able to show that the measured axial strain rates agreed reasonably well with those based upon a simple theoretical model. Pellett suggested that the air jet velocity measured the CFDF extinction limit more directly than the fuel velocity, and that the relevant velocity for characterizing extinction phenomena was the air input velocity along the stagnation streamline.

Numerical developments in modeling CFDF until recently have universally assumed a stagnation-point potential flow (known as Hiemenz flow) superimposed on a flame reaction region.[2,13,14,16,18] That is, by assuming constant density and irrotational motion, the flow field upstream of the flame reaction region can be characterized by a constant velocity gradient,*a*. The upstream velocity field is determined by the axial velocity ($u=-2az$) and the radial velocity ($v=ar$), where z and r are the axial and radial distance from the stagnation point (SP). This Hiemenz velocity profile is then used as the freestream boundary conditions on the flame reaction region, which is assumed to be a thin layer region. This model further assumes that: radial variations in all flow field variables are negligible, the radial velocity v is linear in r ; axial pressure variations are negligible. These assumptions together with the thin layer approximation result in an ODE Boundary Value Problem of the boundary layer type. This model is usually solved on a finite domain which forces the Hiemenz freestream velocity profile (at a constant strain rate) to be at a finite distance from the SP, which is not consistent with most experiments reported. That is, the constant strain rate, a, in the freestream is specified, and therefore, the axial velocity gradient is constant at the specified boundary point position relative to a specified SP. Thus the specified strain rate, a, is the single key parameter that will characterize the flow field, and determine the flame extinction.

In another recent development of the CFDF modeling, Kee and et al[17] model the freestream boundary conditions, approximated as plug flow, by introducing a streamfunction $\psi(z,r)=r^2U$, which will satisfy the mass continuity equation. The streamfunction is defined such that the flow field radial velocity varies linearly in r while the axial velocity depends only on the axial distance z. Also, this model further assumes that the flow field temperature and species mass fractions are functions of axial distance z alone. These assumptions together with the streamfunction introduced also reduce the CFDF momentum equations to an ODE Boundary Value Problem, however, with the boundary conditions relaxed. This model differs from the one above in that it assumes the upstream axial velocity to be uniform with zero radial velocity component, and the upstream strain rate is not specified. Instead, the upstream velocity is specified, and the upstream boundary point is calculated with the strain rate as an eigenvalue of the solution.

Currently, the above models have been less than satisfactory in predicting experimental extinction conditions reported so far. This work will experimentally assess some of the assumption and approximations via laser Doppler anemometry measurements of the velocity field.

1.1.2 Laser Doppler Anemometry

In 1964, Yeh and Cummins[23] demonstrated the use of coherent light sources (lasers) to measure fluid velocity by observing the Doppler shift in the laser light frequency, scattered from a particle moving with the fluid. Since then, laser Doppler anemometry has become a very powerful measuring technique for fluid flow investigations. There are three different modes of operation of a LDA : (1) reference beam, (2) dual beam or fringe, and (3) dual scatter mode. Each mode can be arranged to collect forward-scattered or backscattered laser light. The dual beam mode of operation was used in this experimental study.

When two beams of laser light pass through a focusing lens, a probe volume is produced by the two intersecting beams. As a particle moves through the region of

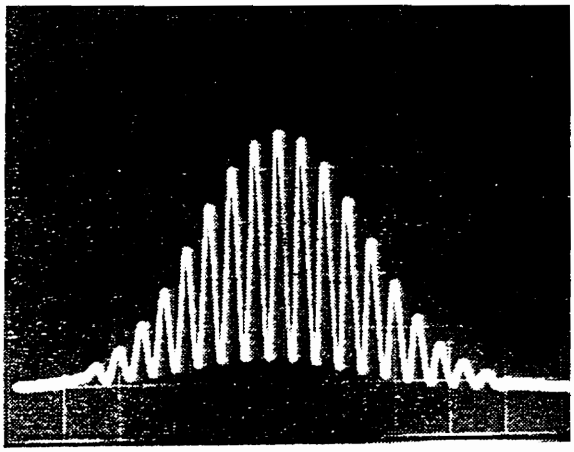

Figure 3 A typical Doppler burst from photodetector before filtering

alternating fringes[24] inside the probe volume it scatters light, the intensity of which varies according to the light intensity variations inside the probe volume. The light intensity variations are caused by the constructive and destructive interferences of the two coherent beams. The fringe spacing is proportional to the incident beam wavelength and inversely proportional to the half-angle between the two intersecting beam. These light intensity variations are detected with photodetectors and it can be shown that the frequency of the detected signals are exactly that determined from the analysis based on Doppler-shift considerations. By Doppler-shift considerations, the change in frequency of the scattered light relative to the incident light, as observed by a stationary observer, is proportional to the flow velocity[25]. In a dual beam mode, the frequency of the Doppler-shifted scattering light is independent of the collecting optics direction. Figure 3 illustrates the detected signal displayed on an oscilloscope.[26]

Detailed descriptions of the other two modes of operation (reference beam and dual scatter), and the principles and applications of LDA are thoroughly discussed in reference[25]. LDA is a practical technique and has substantial advantages over the mechanical probes (hot wires, pitot tube, etc). It is non-intrusive, not affected by the flow field temperature or density, and is directionally sensitive. Also, LDA does not require constant recalibration. Thus, the LDA is ideally suited for measurements in combusting flow fields.

2. EXPERIMENTAL

Overview

The purpose of this chapter is to describe the experimental hardware and procedures used for the optical measurements. The chapter begins with a description of the hardware used for the experiment. The next section explains the pre-experimental procedure, that is, the set-up of the LDA and OJB systems, aligning these two systems and determining the OJB centerline. The final section is a description of the procedure used for velocity measurements in this experiment.

2.1 INSTRUMENTATION

2.1.1 OJB system

The OJB system consisted of two long mutually opposed circular tubes of 7 mm diameter (D) each in a vertical orientation, as shown schematically in Figure 4. The fuel (bottled hydrogen) and diluent (bottled nitrogen) were supplied through the upper tube, while the oxidizer (bottled air of grade D) was supplied through the lower tube. All the bottled gases were supplied by Airco. The reverse orientation of the tubes did not

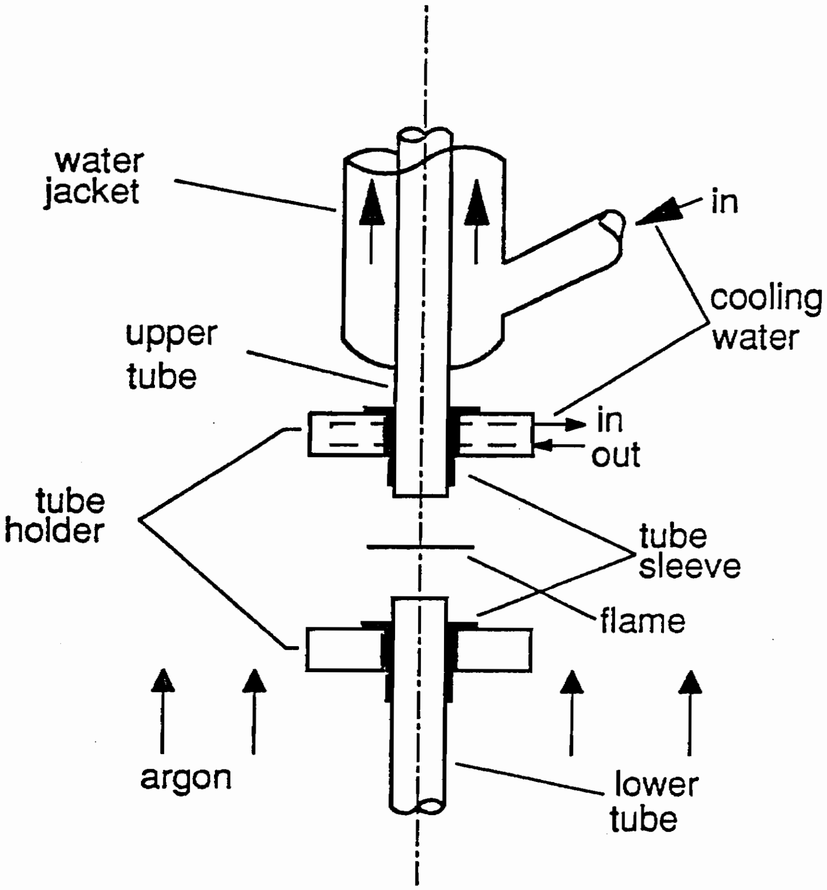

Figure 4 A schematic of the OJB system

produce a flat dish-shaped flame and was considered unsuitable for this study. Both the upper tube and lower tube were supported and aligned by an aluminum fixture (tube holder). The upper tube was covered and cooled by a water jacket and a tube sleeve. This served to prevent any pre-heating of the fuel by the heat released from the combustion region. The water jacket covered and cooled the upper tube ~56 mm from the jet lip, and extended well past the OJB box fibrous cover, where the hot products were diffused into the ambient surrounding. The tube sleeve was about 44 mm long, and covered the upper tube ~2 mm from the jet lip upward, and was cooled by circulating tap water through the fixture. Both the aluminum fixture and water jacket were cooled with a continuous flow of tap water. The cooling water was occasionally checked for any temperature rise, to ensure proper cooling. Both the upper and lower tubes were at least 60D long, thus ensuring that the flows in both tubes were fully developed for all tested flow rates. The velocity profiles (seeded air-side) were verified to be parabolic at the tube exits, as shown in Fig. 5 and 6 for the two different air flow rates investigated. The tube holder restricted any radial movements of the tubes, but permitted axial adjustments in tube separation. The OJB system was enclosed in a polycarbonate box which was continuously purged with argon supplied through a fibrous diffuser pad at the bottom of the OJB box. The open top of the box was partially covered with fibrous material to allow the combustion products to escape and also to ensure that the pressure inside was atmospheric. It was found that without the top cover the flame region was disturbed, due to unwanted reaction of the hydrogen with the atmospheric air. In addition, the fibrous top cover reduced the flow of outside ambient air into the burner box. The introduction of ambient air must be minimized to avoid disturbance to the flame zone via undesirable

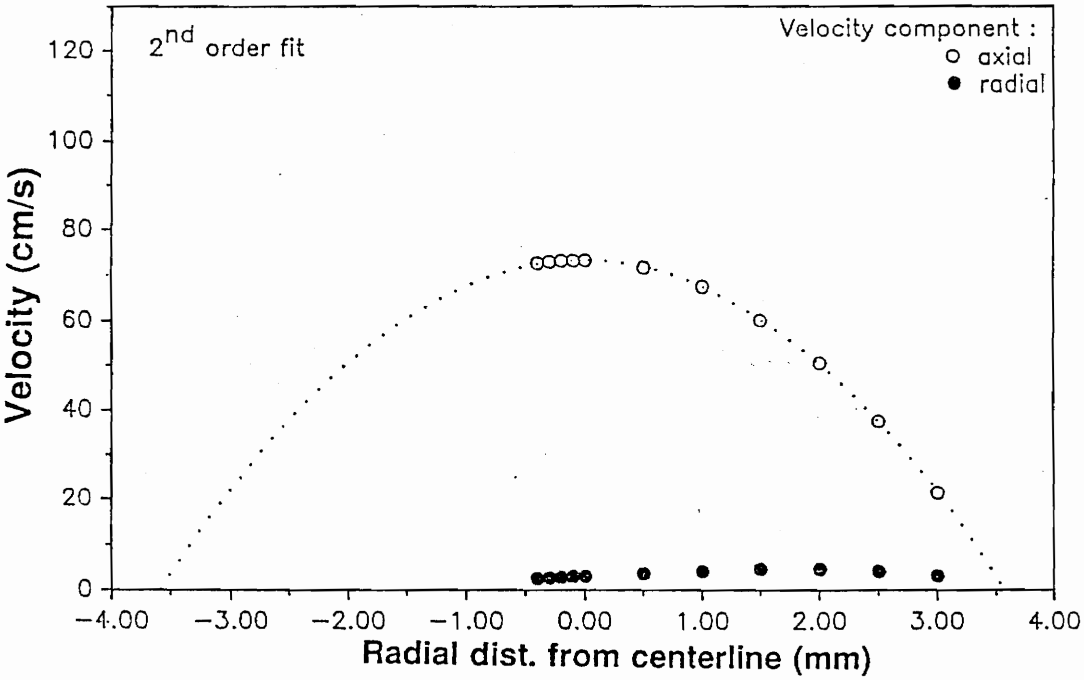

Figure 5 The measured velocity profile at the air jet exit @lower flow case

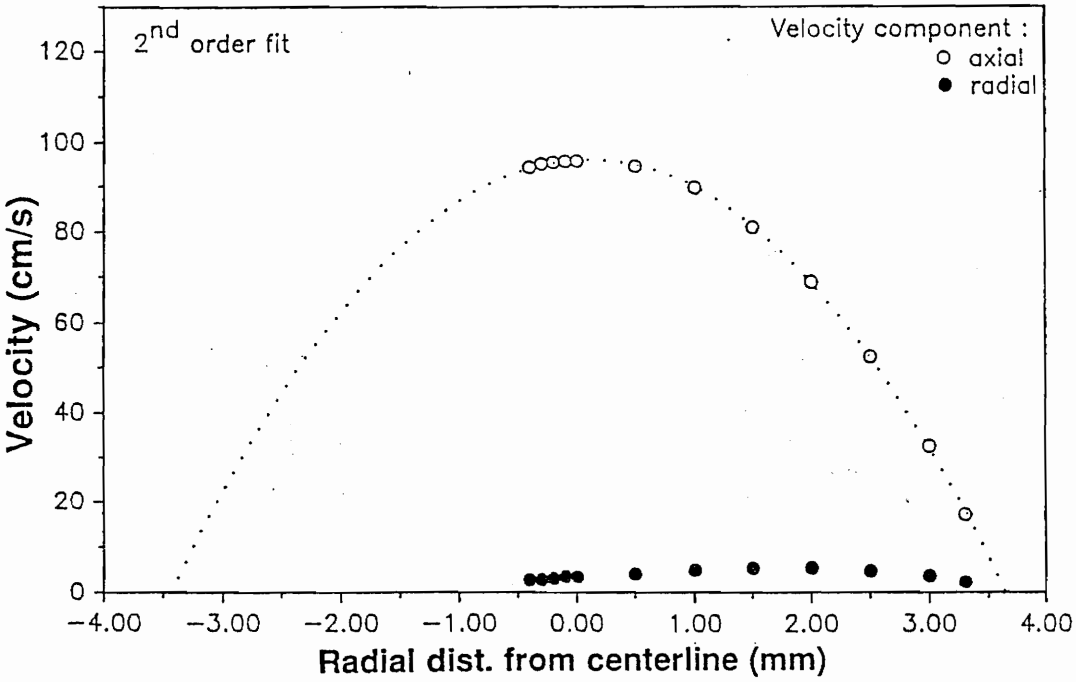

Figure 6 The measured velocity profile at the air jet exit @higher flow case

fluid currents into the box.

The argon-purging prevented any undesirable secondary combustion of the excess fuel outside the central impingement zone. This also improved the visibility of the central flame, decreased local heating and reduced the effects of buoyancy near the flame periphery. Also, H_2O product from the combustion region condensed on the inside wall of the box without this argon-purging. However, it was observed that too much argon flow affected the flow field and caused "jittering" of the flame. Thus the right level of argon flow was very important, and was adjusted carefully by observing the flame and any mist forming in the box. Figure 7 is a photograph of the OJB system showing: the polycarbonate enclosure box; both the upper and lower tubes were at least 60D long, with the upper tube held in place by the clamp shown, while the lower tube was held in place by a set screw; the copper tubing carried the argon into the bottom of the box.

1. Flowmeters

Figure 8 is a schematic of the gas supply system for the OJB system. The gas flow pressures were first throttled down by the pressure regulators to a pressure of 30-60 psi, while the flow rates were regulated and measured with electronic Hastings flowmeters (Model 200A), which measure the flow rates via temperature difference across the flowmeters . The flowmeters were used to measure the flow rates of air, hydrogen, and nitrogen independently. The flowmeters have a digital readout and are capable of

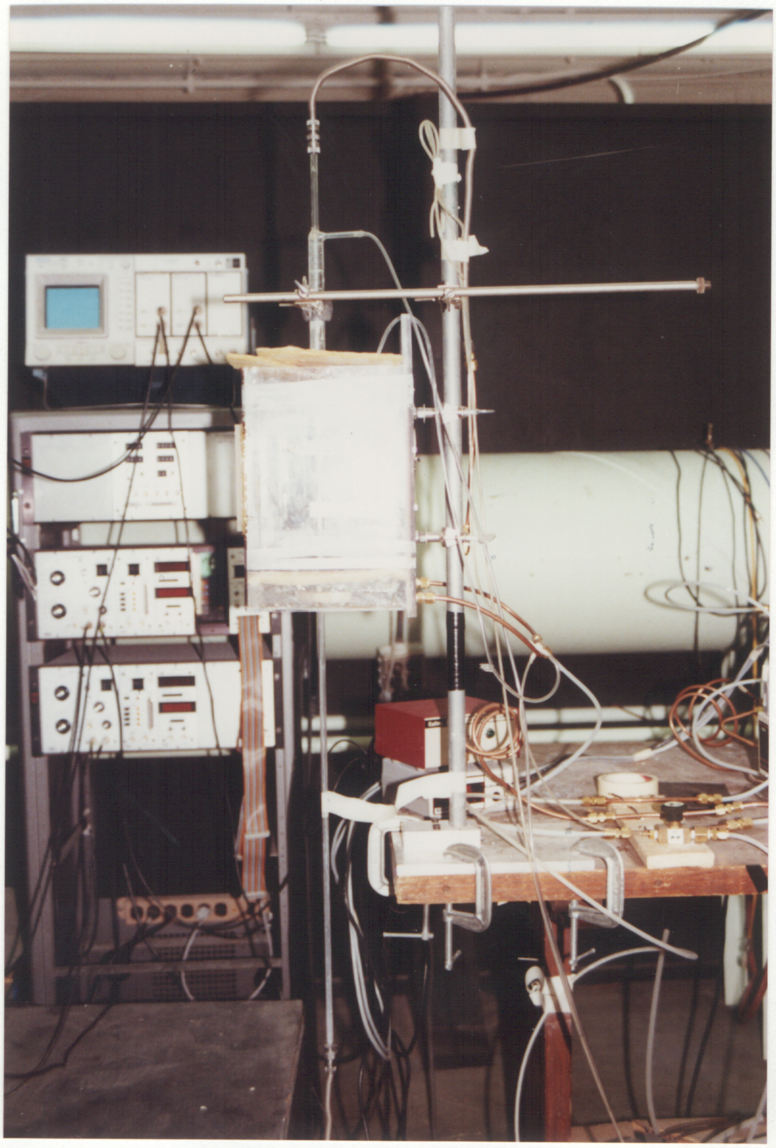

Figure 7 A photograph of the OJB with the enclosure box

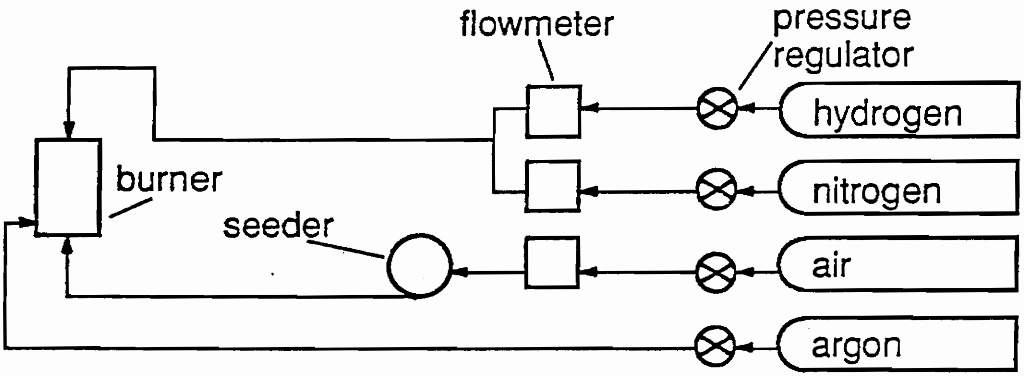

Figure 8 A schematic of the gas supply system for the experiment

measuring down to one one-hundredth of a standard liter per minute (SLPM), and up to a maximum flow rate of 5.00 SLPM. The flowmeters were powered by the Hasting power supply, Model PR-4A. All the flowmeters have an accuracy of ±1% at the maximum flow rate, and were calibrated by Hastings. Zeroing of the flowmeters was done prior to each velocity measurement.

2. Seeder

LDA relies upon the availability of particles to scatter the incident laser light. In order to ensure accurate measurements of the fluid velocity, it is necessary to have the particles "track" the flowing fluid as closely as possible. Thus, the particle size has to be as small as possible to accurately represent the fluid flow, yet large enough to scatter sufficient light for the measurements. In this experiment, the particles were generated by supplying the metered oxidizer (air) through a "fluidized bed" seeder, designed at VPI&SU. A schematic diagram[27] of the seeder is shown in Fig. 9.

A chemically stable material, Al_2O_3 (Union Carbide, grade Linde B), was considered appropriate for this H_2-air combustion experiment. A small amount of the material (20-30 g) was introduced into the bottom chamber of the seeder. The seed was dispersed by directing flow through three small perforated tubes connected to a stirrer rod above the seed bed, while the rod was rotating at low speed. The seeder is capable of operating at chamber pressures of up to 250 psig[27] with an estimated particle generation rate of

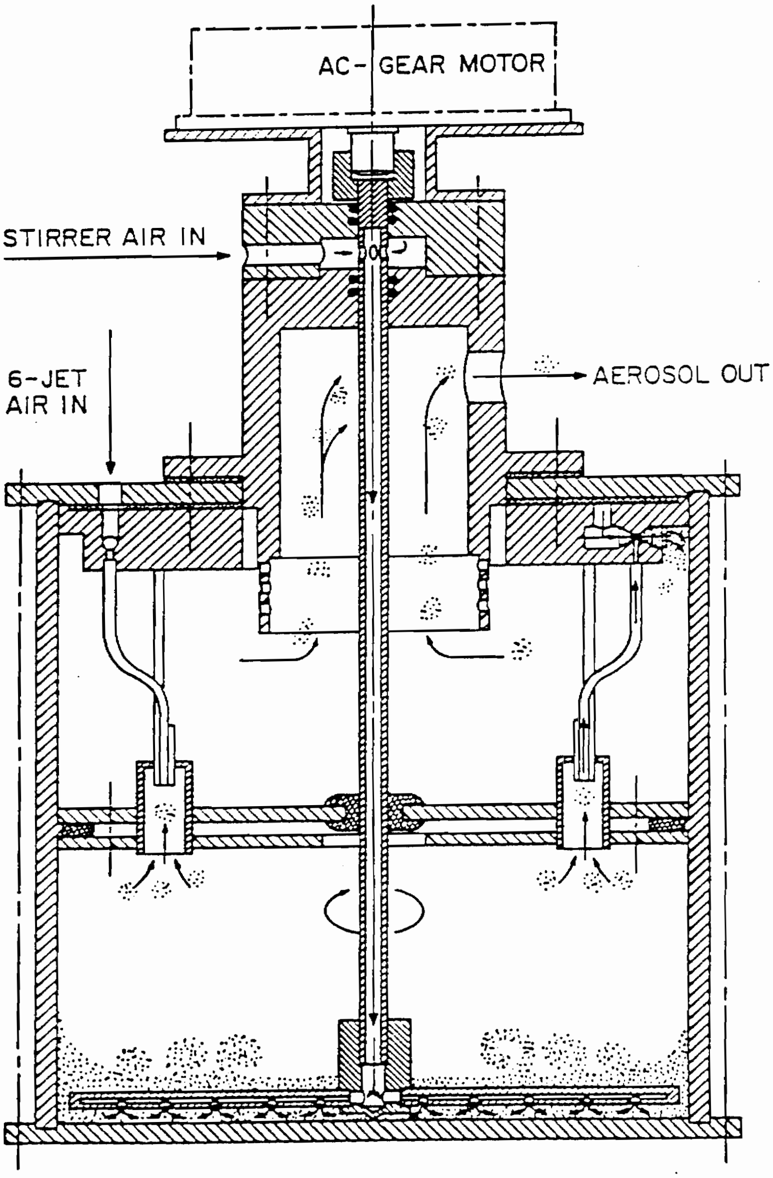

Figure 9 A schematic diagram of the seeder used

approximately $6x10^6$ s^{-1}. Due to the low flow rates used for this experiment, all of the air flow was directed through the bottom chamber to provide particles for the LDA measurements. Only the air-side velocities were measured in this experiment.

Particle samples were collected by placing pieces of microscope cover glass inside the OJB box. Air flow rates (cold flow) of ~0.7 and ~1.0 SLPM were passed through the operating seeder into the box with the top covered, and left overnight. The particle sizes were determined by inspecting the collected samples with a scanning electron microscope. Figures 10 and 11 are photographs of the samples collected at the low and high flow rates respectively. For the lower flow rate case, the average particle size was about 3 µm in diameter with no particles above 10 µm size. While at the higher flow rate case, the average particle size was about 5 µm with no particles above 10 µm. The particle lags associated with the above size range are discussed in section 3.1. However, no other independent confirmation can be made about the true representation of the actual seed size or distribution as shown by those photographs. Figure 12 is a photograph of the seeder used in this entire experiment, showing the gas lines from the gas supply system.

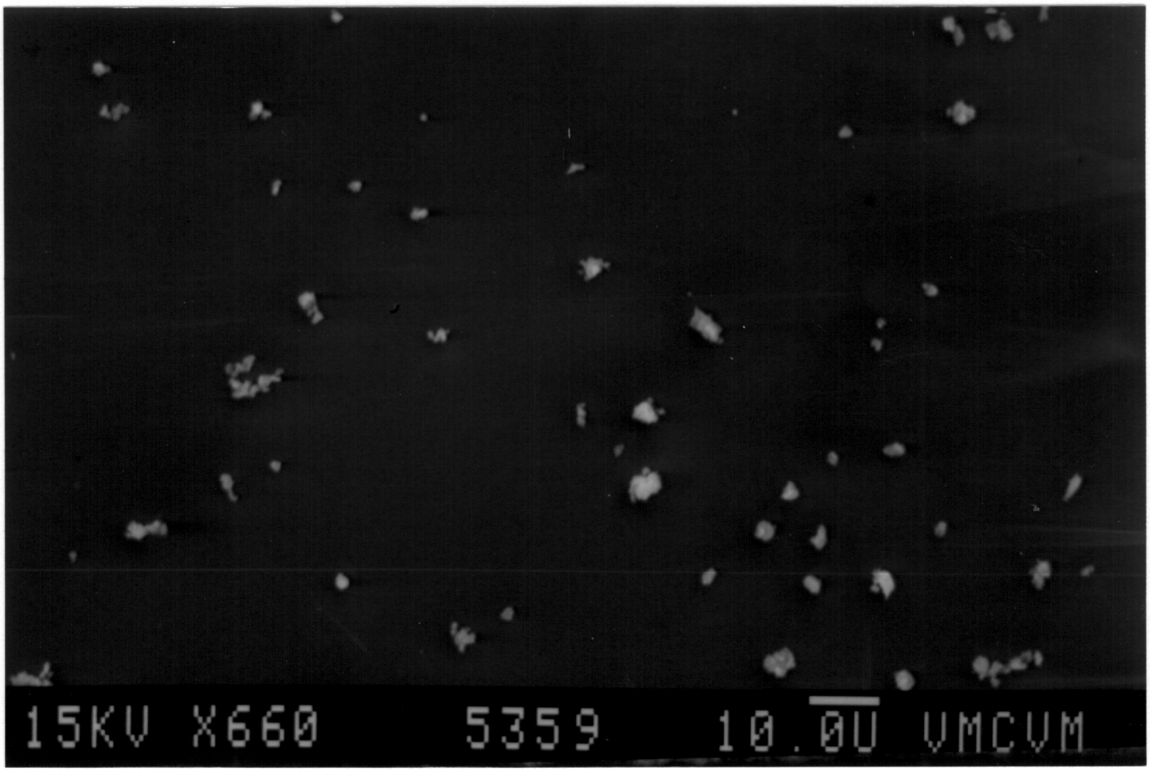

Figure 10 A photograph of the seed sample @lower flow case

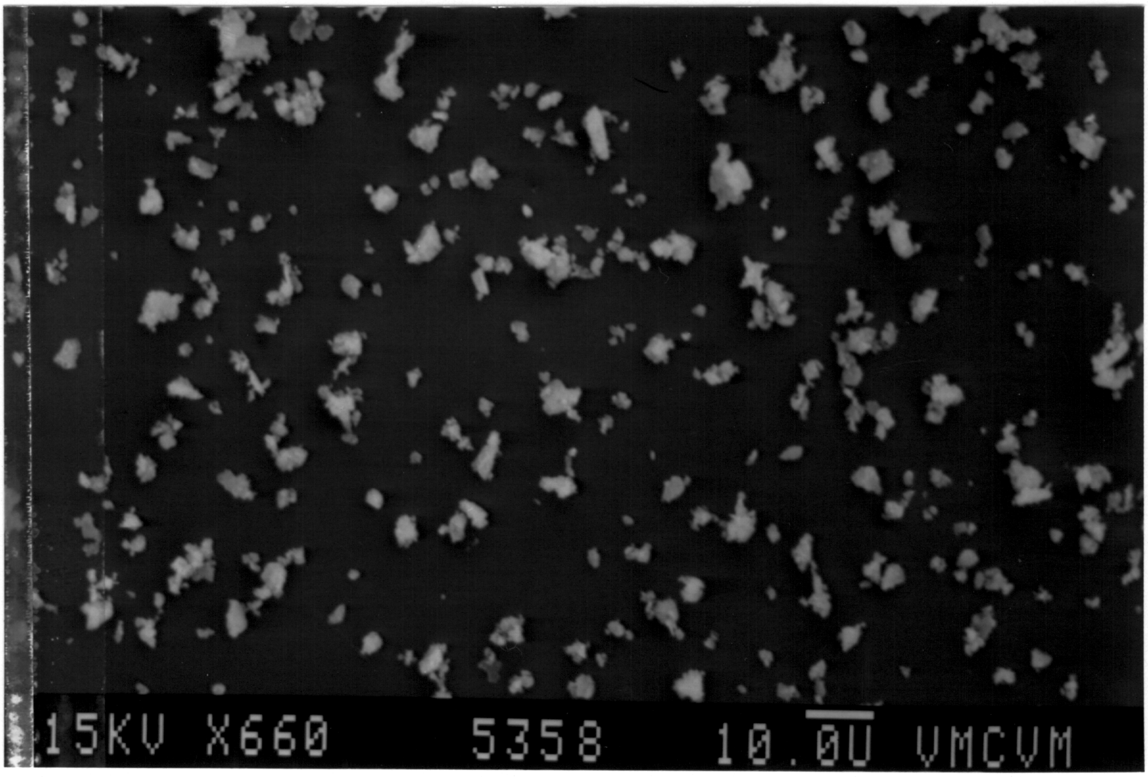

Figure 11 A photograph of the seed sample @higher flow case

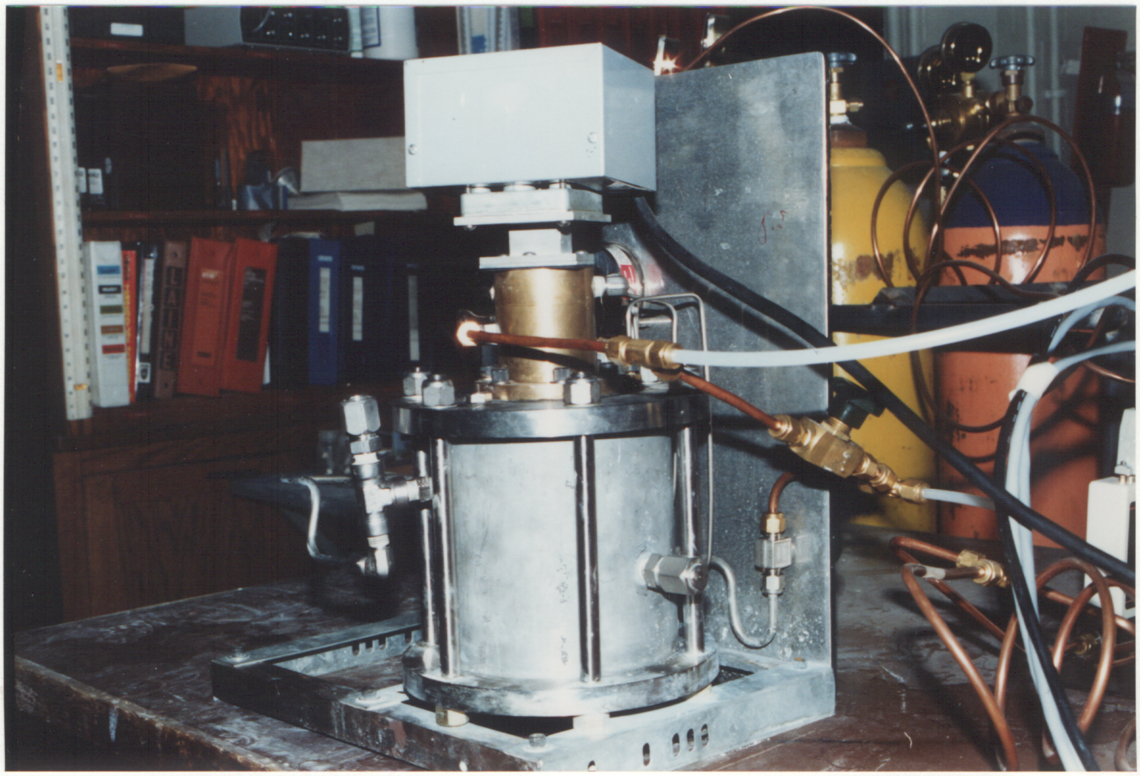

Figure 12 A photograph of the seeder used for this experiment showing its connection to the gas supply system

2.1.2 LDA system

1. LDA operation

The velocity measurements were made using a two color, dual-beam, laser Doppler anemometer, in off-axis back-scatter mode. This dual beam system measured velocity components orthogonal to its optical axis and was aligned such that the two velocity components corresponded to the axial and radial velocity components of the axisymmetric OJB flow field. The back-scatter arrangement was used due to the geometry of the OJB system. Figure 13 illustrates the basic components of the LDA system.

A 8 watt argon-ion laser (Lexel Model 95) was employed and provided approximately 0.5 watt each on both the 514.5 nm (green) and 488.0 nm (blue) lines. These two lines were separated by the use of a dispersing prism, and each line was subsequently split into two beams of approximately equal power. One beam of each of the pairs was then passed through a Bragg cell, which optically shifted the beam by 40 MHz. Each pair of beams was then passed through a common transmitting optics and focused to produce the probe volume. Within the probe volume, the two coherent light beams of each pair intersected and constructively and destructively interfered to produce a fringe pattern of alternating bright and dark bands. These fringe patterns for the two separate channels were orthogonal to each other and normal to the transmission optical axis. The fringe spacing for the green line was calculated to be d_f=7.9 μm ±1.8%, while the blue line yielded a fringe spacing of d_f=7.3 μm ±2.6%. Detailed calculations of the fringe spacing and its uncertainty can be found in Appendix A.

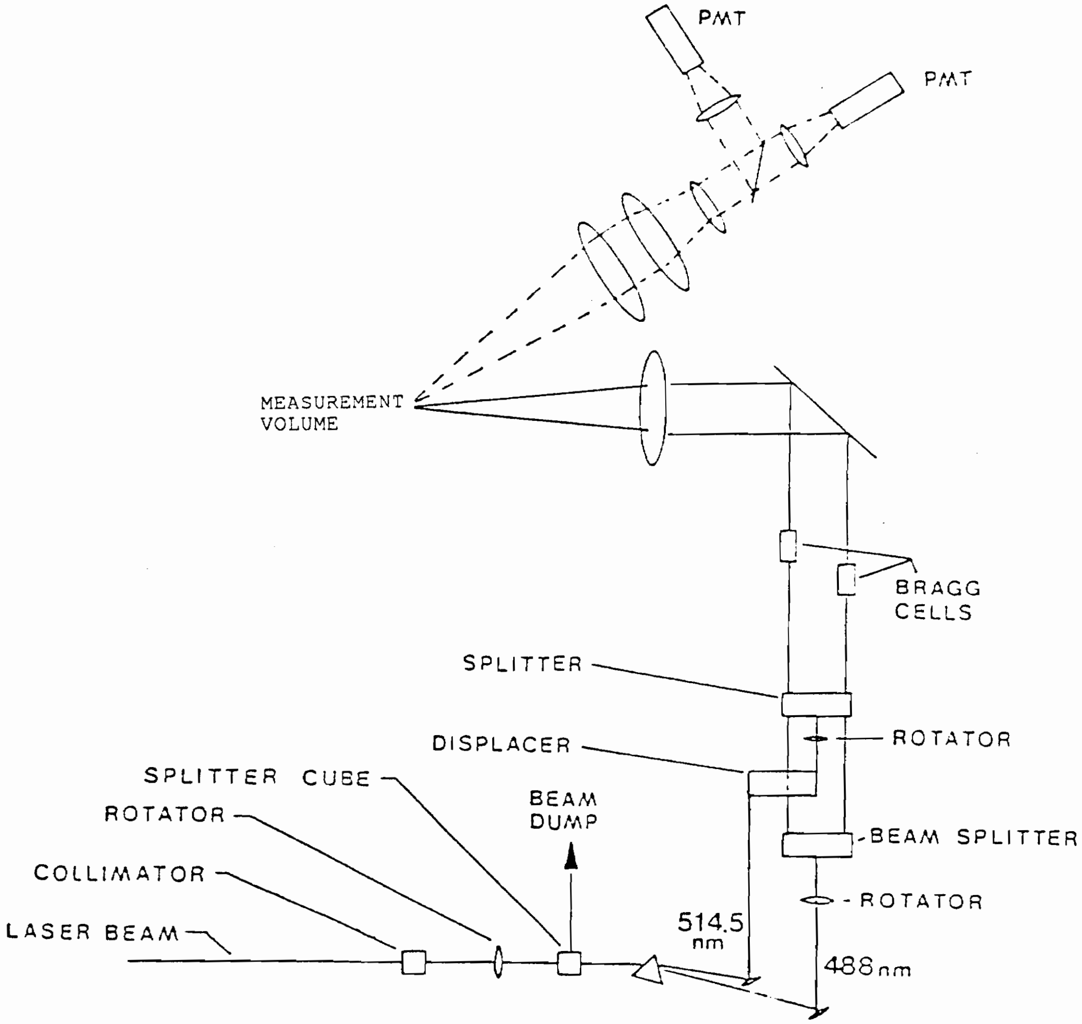

Figure 13 A schematic of the LDA system

The collection optics were mounted at approximately 22° off-axis to the incident beams. The resulting measurement volume was estimated to ~0.064 mm in diameter by ~0.15 mm long.[28] The signal from each photodetector (TSI Model 9162) was downmixed to provide effective frequency shifting of 0 to 10 MHz. The signal after downmixing was further filtered by the signal processor to remove both the pedestal (low frequency) and noise (high frequency). Figure 14 shows a Doppler burst that has been band-pass filtered by a processor.[26] Careful setting of these filters is very important in narrowing the frequency bandwidth without attenuating the Doppler signal. Counter-based (TSI Model 1990C) signal processing was used with a clock speed of 1 GHz. Coincidence mode operation was employed with the coincidence window set at 10 µsec (minimum available). The filter settings, for both channels, were 300 kHz and 2 MHz for the low and high limits respectively. A DEC micro PDP11 system was used to run the data acquisition software. Data was collected in continuous mode. For each spatial location in the measuring flow field, 1024 simultaneously occurring LDA events in the blue and green channels were collected.

The error propagation and uncertainty analysis associated with this particular LDA system used in this experiment can be found in Appendix A.

2. Frequency Shifting

Frequency shifting was accomplished with an optical Bragg cell (TSI Model 9182) powered by a electronic mixer/power supply (TSI Model 9186).

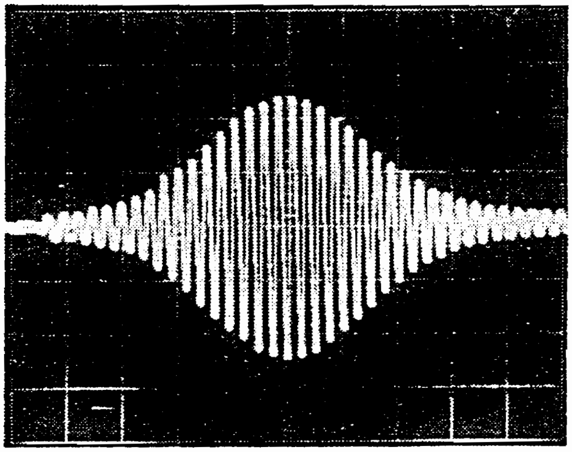

Figure 14 A typical Doppler burst that has been band-pass filtered

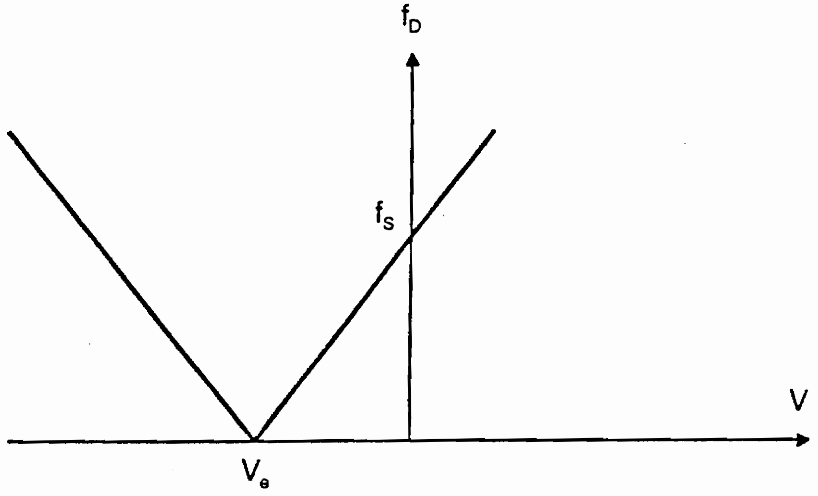

Figure 15 A graphical illustration of frequency shifting

The signal out of the PMT, with the Bragg cell in operation, has a frequency of f_v±40 MHz where f_v is the particle frequency, and this frequency range is usually too high.[29] The maximum measured Doppler frequency was on the order of 0.7 MHz. The built-in downmixer is capable of providing an effective frequency shift of 0 to 10 MHz. The effective shift frequency used in this experiment was set at 500 kHz. Figure 15 graphically illustrates the effect of frequency shifting to the Doppler frequency observed. For example, if the expected maximum reverse flow velocity is V_e=-10 cm/s in a fringe spacing of 7 μm (f_D=14.286 kHz), then the frequency shifting is set at 15 kHz with a corresponding V_e=-10.5 cm/s. That is, any reverse flow velocity of greater than -10.5 cm/s can not be measured at all. For example, if a flow velocity of V=-12 cm/s is present in the flow, the detected Doppler frequency will be f_D=2.143 kHz, which will be the same Doppler frequency observed from a flow velocity of V=-9 cm/s. Though it is often said that frequency shifting can eliminate directional ambiguity, one need to have an estimate of the possible reverse flow magnitude before setting the frequency shift.

2.2 PRE-EXPERIMENT PROCEDURES

This section describes several important procedures which were required prior to the actual data acquisition within the OJB. It consisted of: alignment of the LDA and the OJB systems; "calibration" of the fringe spacing, d_f; improving the signal quality by reducing noise or internal reflections; and finally determining the centerline of the OJB system.

The LDA system used for this work was mounted on a traversing system (TSI Model 9500) which included the optical table (TSI Model 9127) and a power supply (TSI Model 9530) with a 3-axis remote control (TSI Model 9533). In this experiment, movements of the traverse table were controlled by the manual 3-axis remote control, though the traversing system is capable of being remotely controlled by computer software. The half-angle of each pair of focused beams was determined with an optical protractor (TSI Model 10935). Figure 16 is a photograph showing the LDA system and its receiving optics mounted on the same optical traverse table. In addition, by projection onto a wall, the orientation of the two separate beam pairs relative to each other was obtained. In this experiment the blue line was oriented to the vertical as determined from a plumb line. That is, the blue line measured the axial velocity component in the OJB, while the green line measured the corresponding radial velocity component. The OJB system was mounted on a table and was stationary, while the traversing optical table gave axial and radial movements.

For the OJB system, the lower tube was used for aligning the system with the true vertical by means of a water-level gauge. From Fig. 5 and 6, the maximum velocity in each flow was shown to be at the center of the lower tube. These centerline velocities should by purely axial with no radial component, assuming fully developed flow and symmetry about the centerline. However, Fig.5 and 6 show a slight nonzero radial

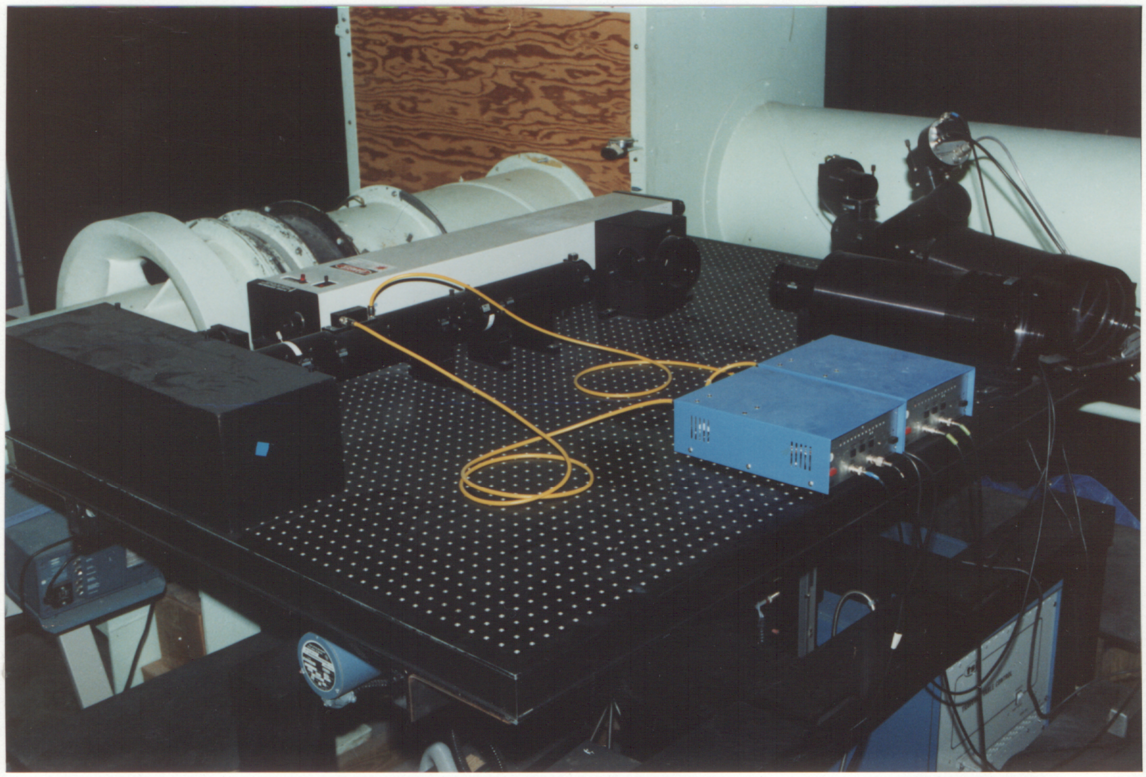

Figure 16 A photograph of the LDA system lay-out with its receiving optics mounted on the same optical table

component at the centerline. These indicate a slight misalignment between the LDA and OJB systems of approximately 2°. No attempt was made to fine adjust the alignment between the LDA and the OJB systems. The upper tube was used for setting the tube separation. The separation distance was measured by means of the laser and the traverse table. The lower tube was tightened in place to the tube holder by a set screw, while the upper tube was free to slide vertically and held in place by a clamp.

The signal quality of the LDA system was checked by providing a seeded flow through the lower tube. Using an oscilloscope (Tektronix Model 11302) the Doppler signals were then observed on both the green and blue channels after filtering by the signal processor. With one beam of each line blocked just after the transmitting optics, the oscilloscope was observed for any spurious Doppler burst signals in both channels, due perhaps to undesirable internal or external reflections. If there was any signal, then that particular line was checked for possible errors. Possible sources of error included: internal reflections in the transmitting or receiving optics; reflections off the burner window or tube holder; misalignment of the photodetector pin-hole; or the filter settings on the signal processor.

The centerline was determined by again using seeded flow in the lower tube. Measurements were taken by first traversing along the *y* direction as indicated in Fig.17. These measurements were then analyzed for the highest velocity location, y_l, since the flow was assumed fully developed and parabolic at the exit. Then another measurement traverse was made along y_l in the *x* direction. Similarly, the highest velocity location, x_l,

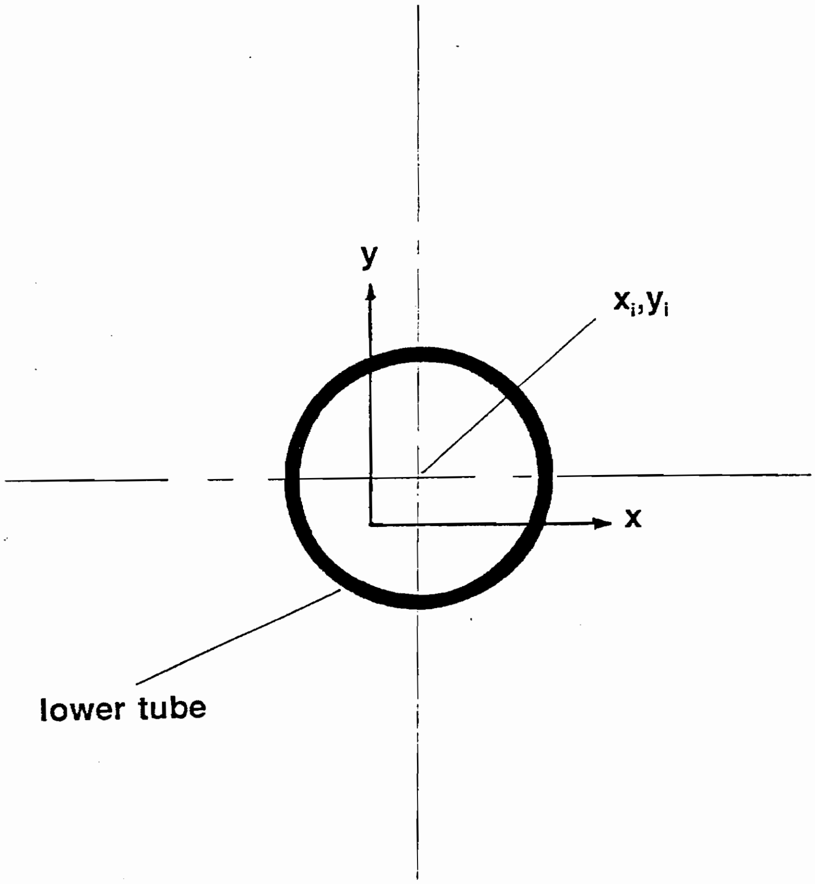

Figure 17 A schematic of the coordinate system used to locate x_i, y_i

was then determined. Hence, the center of the lower tube was assumed to be located at x_l and $y_{l.}$.

Though it is often said, the LDA does not need calibration, it is recommended that the fringe spacing, d_f, determined from the protractor method, be checked by using another independent measurement of velocity. In the present case, a seeded flow was passed through the lower tube, and LDA measurements were taken just above the jet lip along the centerline. The ambient pressure (P_i) and temperature (T_i) were also taken for calculations. The flowmeters, as calibrated by the manufacturer, display volumetric flow rates at standard conditions (STP i.e. T=273K, P=760mmHg). Therefore, the actual volumetric flow rate (V_i) adjusted to the actual ambient conditions is given by:

$$V_i = \frac{P}{P_i} \frac{T_i}{T} V \tag{1}$$

From Fig. 5 and 6, the calculated flow rate V_i, using the above equation, for each case was found to be approximately 4-5% higher compared to the flow rate calculated from the LDA measurements (For a parabolic flow, $V_{max}=2V_{ave}$). However, an uncertainty analysis of the above equation shows an estimated uncertainty of 2.4%-2.8%, by and large, contributed by the uncertainty from the flowmeter ($\Delta V=\sim2.4\%$). This error was approximately of the same order of magnitude as the uncertainty in the LDA system used, as estimated in Appendix A.

2.3 EXPERIMENTAL PROCEDURES

2.3.1 Velocity Measurement

The velocity component measurements of the CFDF were taken with the LDA system aligned with the OJB system as shown in Fig.18. z is the axial coordinate corresponding to the axial velocity component of the oxidizer flow (positive upward from the exit of the oxidizer tube) and r is the radial coordinate corresponding to the radial velocity component (r=0 on the centerline). The reference z=0.00 mm was actually 0.50 mm above the lower jet lip. As described in the previous section, the alignment of the LDA system to the OJB centerline was first determined before any CFDF measurements were made. A photograph of the alignment is shown in Fig.19, which also shows both the transmitting optics and the off-axis backscatter receiving optics. The tube separation was set at approximately 10 mm (~1.5D) throughout the entire series of experiments.

Two different sets of flow rates were used in this work; in the low flow rate test, a hydrogen flow of ~1.00 slpm with a nitrogen (diluent) flow of 0.210 slpm was used, and the corresponding oxidizer flow to center the flame between the tubes. The higher flow rate test used again ~1.00 slpm of hydrogen with a nitrogen flow of 0.500 slpm and a corresponding oxidizer flow to center the flame. These flow rates are uncorrected, as obtained from the flowmeter readouts. The actual flow rates are determined using conversion multipliers for both the hydrogen and nitrogen flows (1.03 for hydrogen, 1.02 for nitrogen, as determined by the manufacturer).

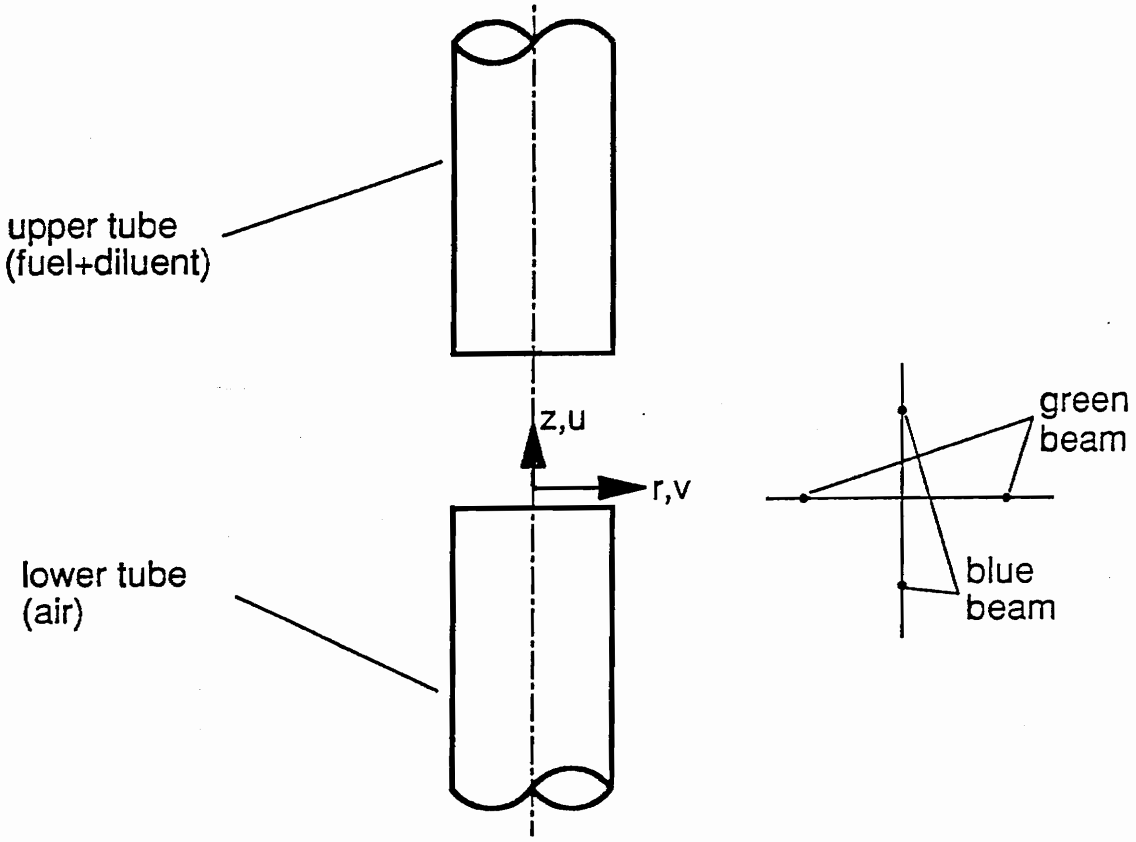

Figure 18 An illustration of the OJB and the LDA coordinate systems

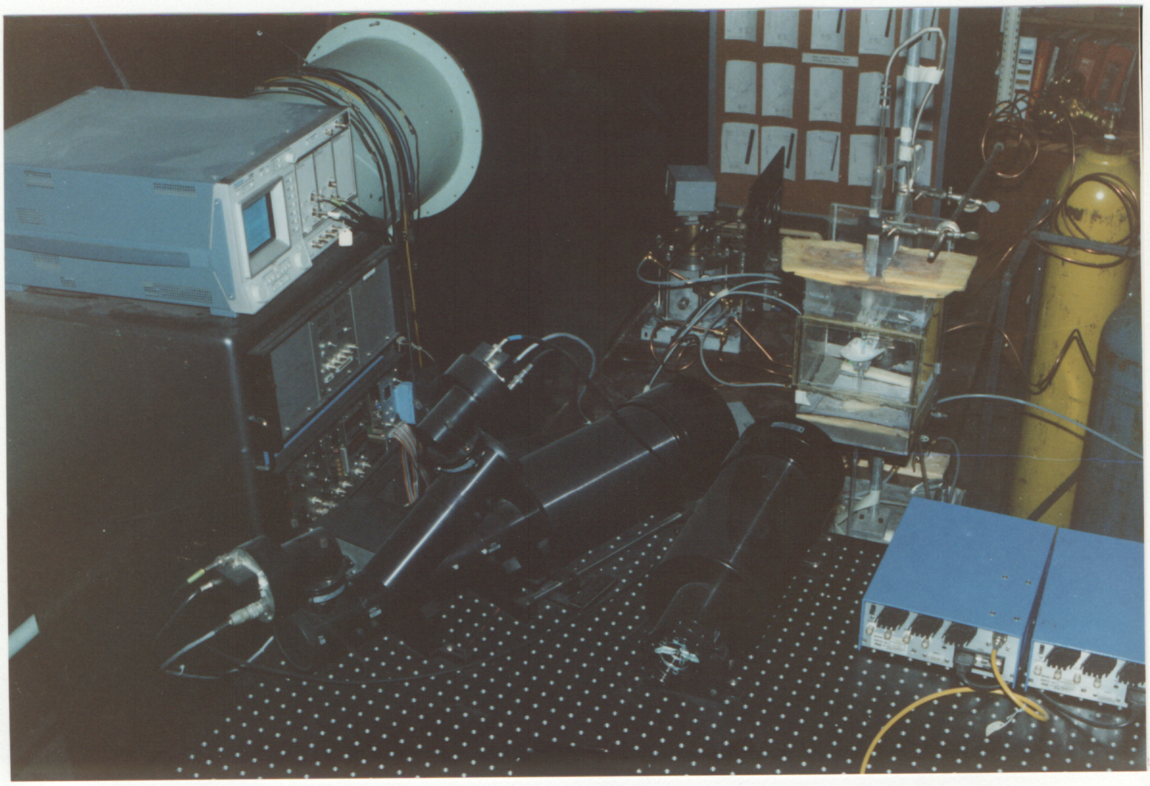

Figure 19 A photograph showing the alignment of the LDA to the OJB systems

For the lower flow rates, the nitrogen was first introduced into the OJB system, for safety reasons, at 0.210 slpm. Then oxidizer and hydrogen were introduced at a very small flow rates, and the CFDF was ignited at this point, again for safety reasons. Then the hydrogen flow rate was slowly increased to ~1.00 slpm, and next the oxidizer flow was slowly increased to balance the fuel and diluent, and center the flame between the tubes. Finally, the argon was introduced into the system in an amount just enough to purge the condensation on the walls of the box. Minor adjustments to the upper tube were made to level the flame.

Stagnation streamline measurements on the air side of stagnation were obtained first, at an interval step of 0.20 mm, from the jet base up through the flame, and close to the stagnation plane. The data acquisition software was modified to acquire the raw data first without analysis. In this way, the time necessary for acquisition was reduced. Measurements were made at ten different axial positions along the stagnation streamline, including one at the oxidizer jet exit plane. For each flow rate and at each particular axial position, measurements were made at nine to ten radial positions, at an interval of 0.50 mm, from the centerline to approximately the tube radius. In this manner, the velocity vector fields of the lower and higher flow rate cases were obtained throughout the air side.

2.3.2 Data Processing

All the raw data was first analyzed (using averaging method) on the DEC micro PDP-11 and then transferred to pc-based spreadsheet software for further processing.

3. RESULTS AND DISCUSSIONS

In this chapter, the velocity measurements for both the lower and higher flow rates are presented and examined in detail. At the lower flow rate case, the air flow rate was ~0.78 slpm, the hydrogen flow rate was ~1.00 slpm, the nitrogen flow rate was ~0.21 slpm, and the ambient conditions were: 700 mm of Hg @ 80°F. At the higher flow rate case, the air flow rate was ~1.02 slpm, the hydrogen flow rate was ~1.00 slpm, the nitrogen flow rate was ~0.50 slpm, and the ambient conditions were: 718 mm of Hg @ 87°F. The first section discusses possible particle lag errors in such flow conditions. The next section of this chapter is on identifying and discussing some of the observed flow features. The last section examines the experimental data to assess published modeling approximations. Figures 24, 26, 28-37, 47 & 49 are plots from data collected at the lower flow rate case; while Fig. 25, 27, 38-46, 48 & 50 are plots from data at the higher flow rate case.

3.1 Particle Lag

In LDA measurement, what is actually measured is a particle velocity. Therefore, the ability of a particle to "track" the fluid velocity in an accelerating flow field affects the accuracy of the measurement. This "particle lag" effect can be very severe in high speed flow[30]. Generally, the particle has to be small in order to accurately follow the flow, but large enough to provide a strong scattering signal. The reported velocity measurements will be of no use, unless the effects of "particle lag" can be estimated.

Figure 20 is a plot of a theoretical stagnating potential flow centerline axial velocity distribution for three different particle sizes (1μm, 5μm and 10μm in diameter). The figure displays particle velocity versus axial position along the centerline. In a stagnating flow, the axial velocity is decreased linearly as the stagnation point is approached (ie. $u=-az$)[31]. From Fig.20, a 1μm sized alumina particle "tracks" the flow accurately, from an upstream fluid velocity of 100 cm/s to stagnation. A 5μm size particle shows some deviations from the 1μm particle track, with the absolute deviation decreasing as the stagnation point is approached. A 10μm diameter alumina particle exhibits serious lag under such flow conditions. Figure 21 is a plot of the particle axial velocity errors relative to the fluid axial velocity in the flow. The 1μm particle indicates a relative error of up to ~1% in the flow, while the 5μm particle indicates a relative errors of up to ~20%. The 10μm particle indicates problems in making any reasonable measurements at all. Both the 5μm and 10μm particles indicate that the particles would penetrate the stagnation plane. Figure 22 is a plot of the theoretical radial velocity distribution for these three particles under the same stagnation flow conditions. All three particles show the linear radial velocity variations as they should in a stagnation flow. Again, the 5μm and 10μm particles show velocity deviations from the 1μm particle. Figure 23 is a plot of the velocity errors of these three particles against their radial position from the centerline under the same stagnating flow field. The 1μm particle indicates a maximum deviation of ~1% from the fluid radial velocity, while the 5μm particle indicates a maximum deviation of ~7% along any radial position from the centerline. The 10μm particle indicates a maximum deviation of ~21%. Figures 20-23 were provided by a student working under Dr. Dancey.

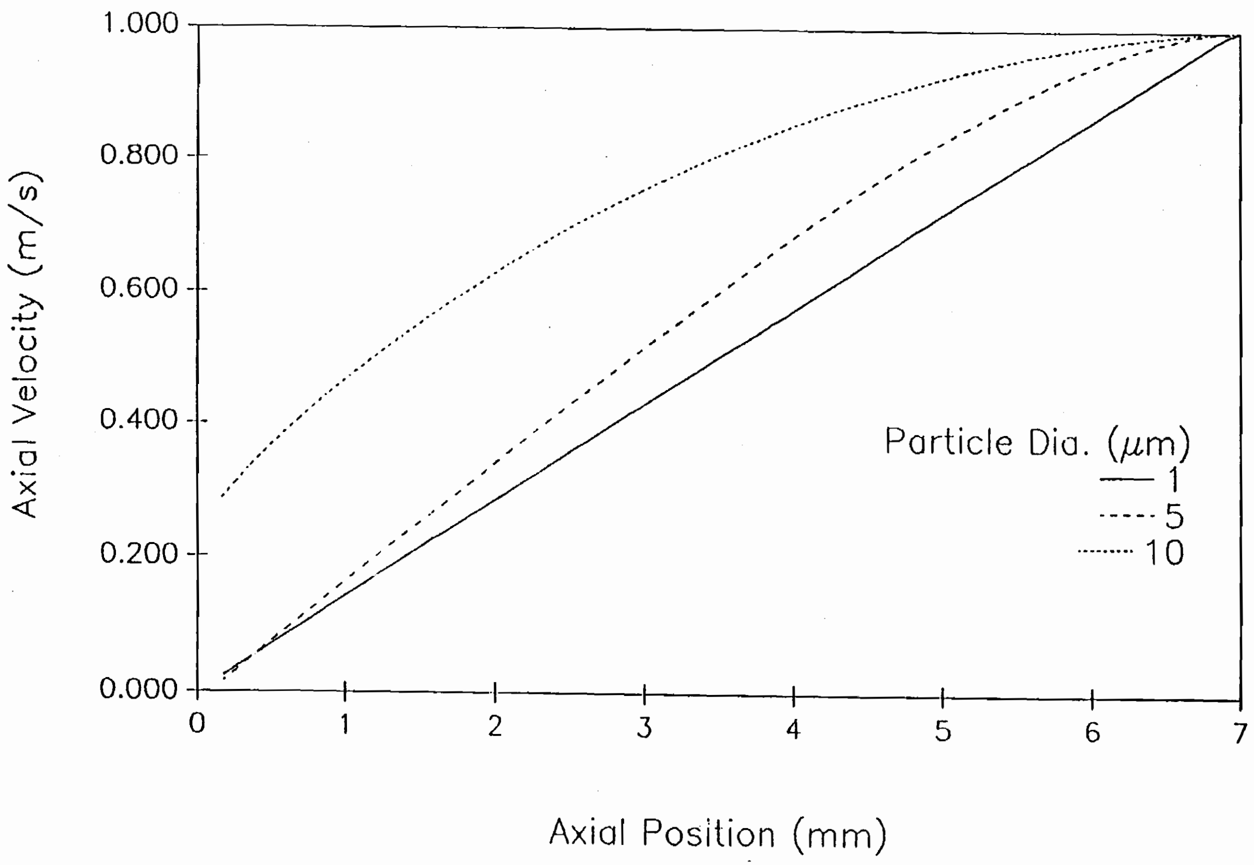

Figure 20 A comparison of axial velocity of the three different sized particles in a stagnating flow field.

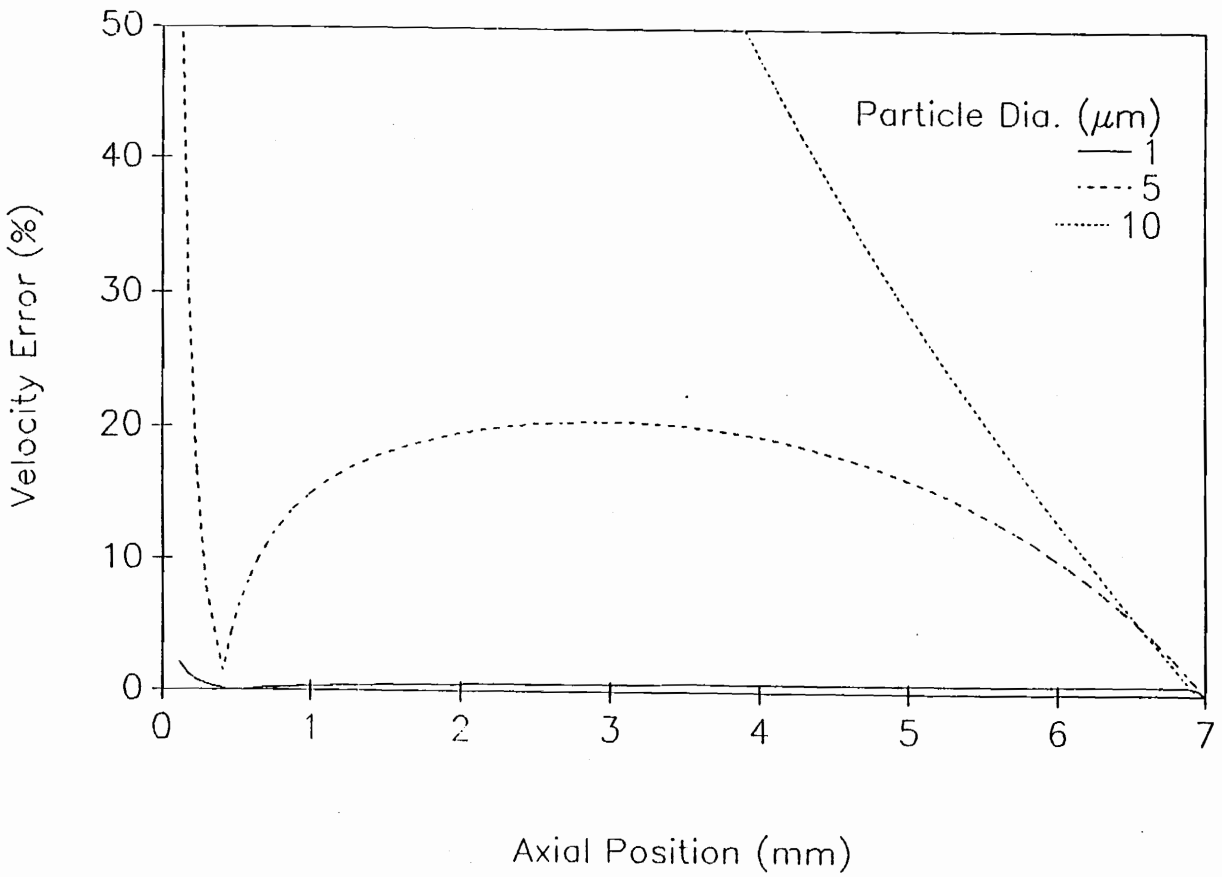

Figure 21 A comparison of the axial velocity deviation of the three different sized particles in a stagnating flow field.

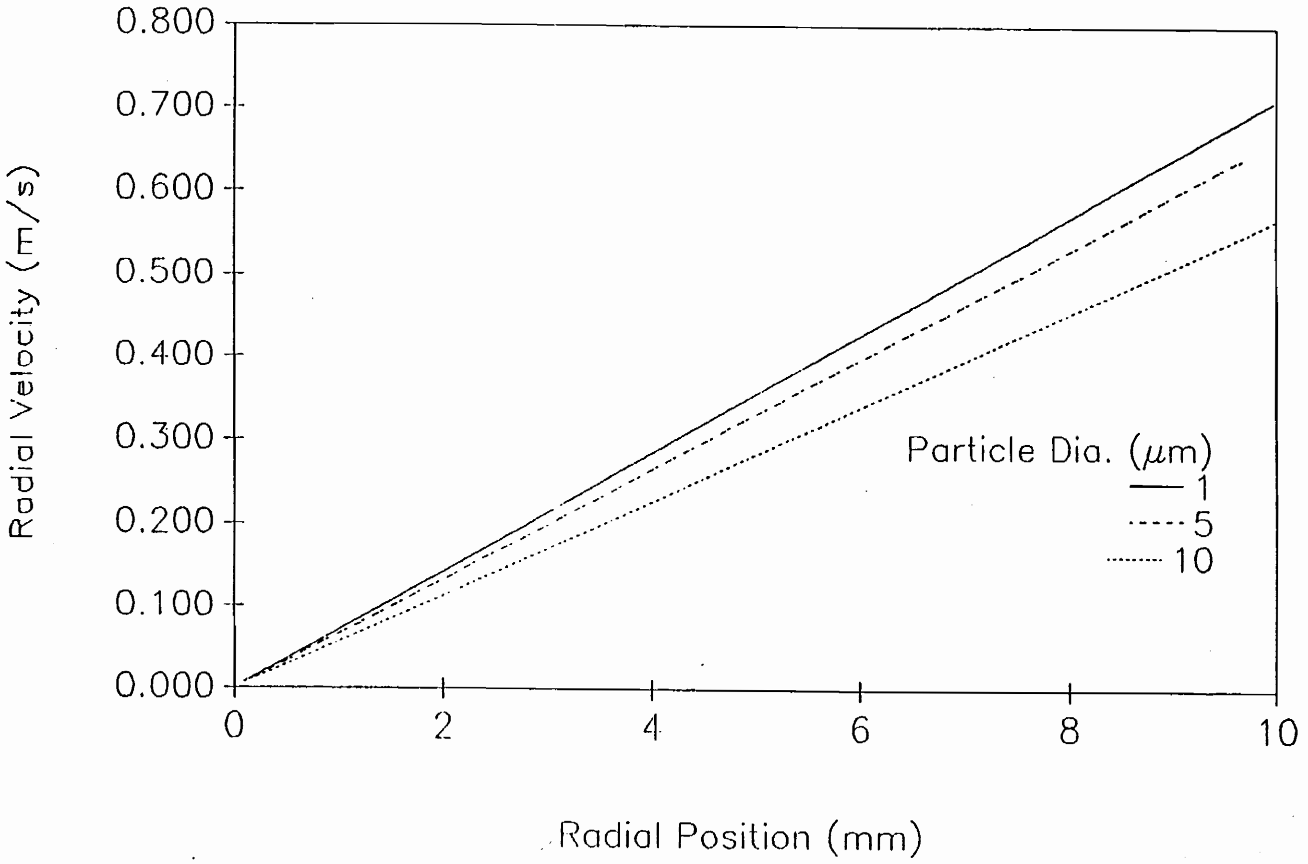

Figure 22 A comparison of radial velocity of the three different sized particles in a stagnating flow field.

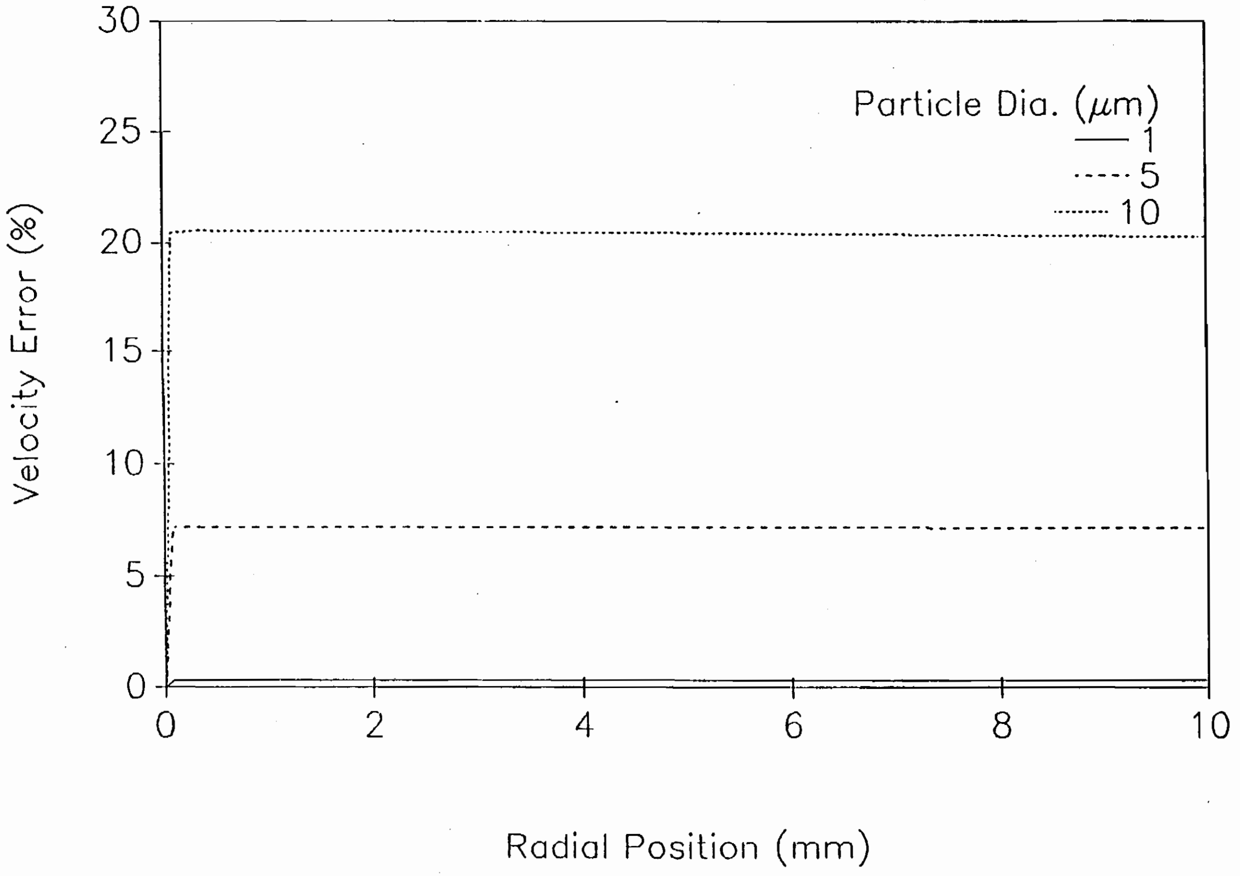

Figure 23 A comparison of the radial velocity deviation of the three different sized particles in a stagnating flow field.

3.2 Measurement Profile

A velocity vector plot of the velocity measurements at the lower flow rate case is presented in Fig.24. Figure 25 is a similar plot for the higher flow rate case. Figures 24 and 25 are vector plots on the air side of the stagnation point, since only the air side was seeded in this experiment. The stagnation point (SP) is found to be located near z= 6.7 mm, for the lower flow rate case, as measured from the air jet reference. The axial reference *z*=0.00 mm was actually 0.50 mm above the air jet lip. For the higher flow rate case, the stagnation point is located near *z*= 5.7 mm, with the same axial reference. From Fig.5 & 6 it is observed that the maximum, centerline velocity, U_{max}, is 74.05 cm/s and 96.19 cm/s for the lower and higher flow rate cases respectively. Figures 24 and 25 are presented using dimensional quantities. For the remaining figures, however, the measured velocity component (axial or radial) $\tilde{u}$ is normalized by its respective U_{max}, the radial distance from the centerline (*r*) is normalized by the tube radius (R=3.5 mm), and the axial distance $\tilde{z}$ (measured from the SP) is normalized by the tube diameter (D). The corresponding supply air strain rate a_{input} is 104.3 s^{-1} for the lower flow rate case, and 135.5 s^{-1} for the higher flow rate case ($a_{input}=U_{max}/D$).

Several qualitative features of the flow fields are apparent from Fig.24 and 25. Beginning from the cold input supply air (that is, at *z*=0.00 mm), the flow velocity distribution appears to be parabolic with a slight nonzero radial component. The stagnation point for both cases can clearly be identified with strong radial acceleration away from SP. Also, the vector plots suggest a slight concavity to the stagnation plane

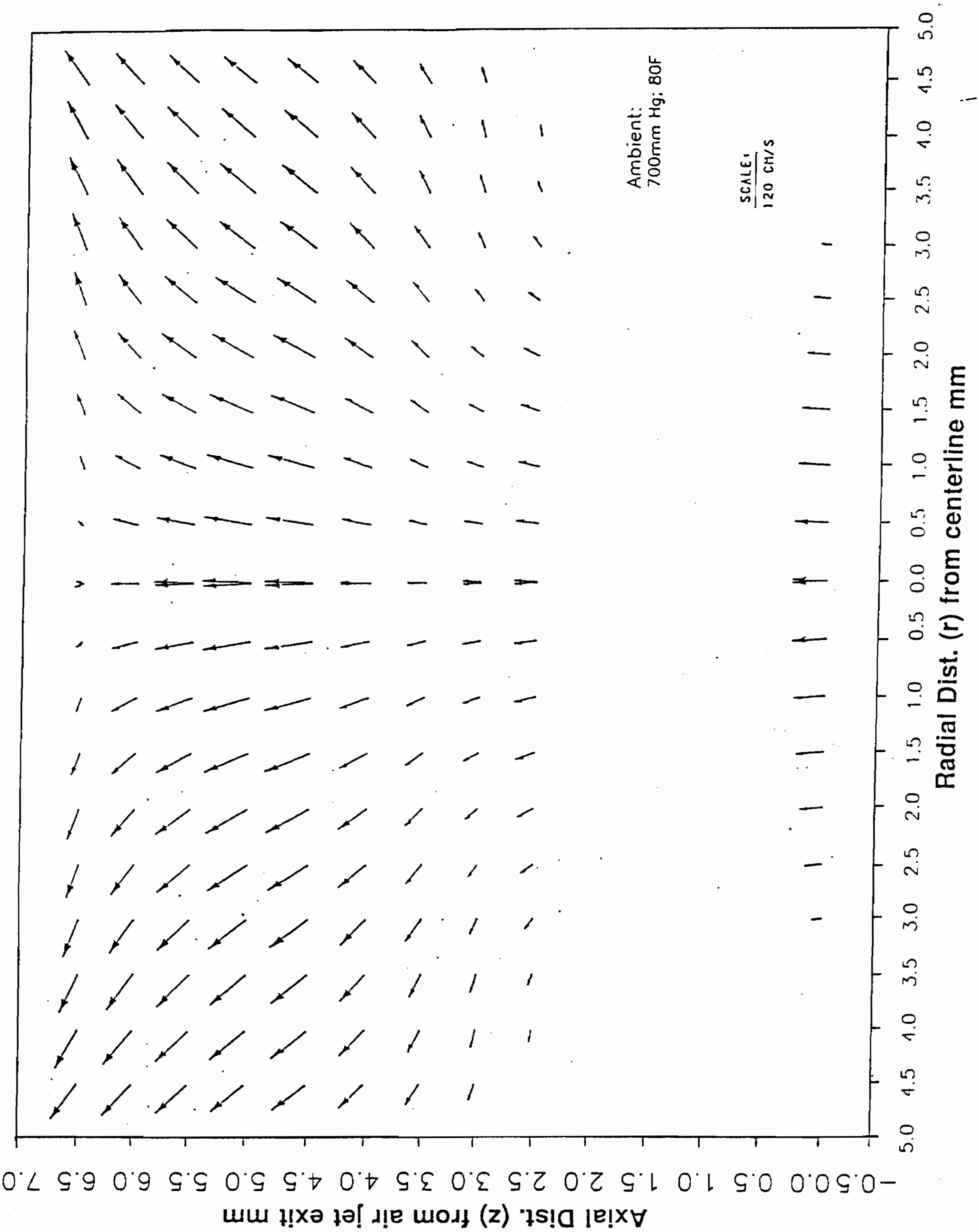

Figure 24 A velocity vector plot of the measured velocity @the lower strain rate case.

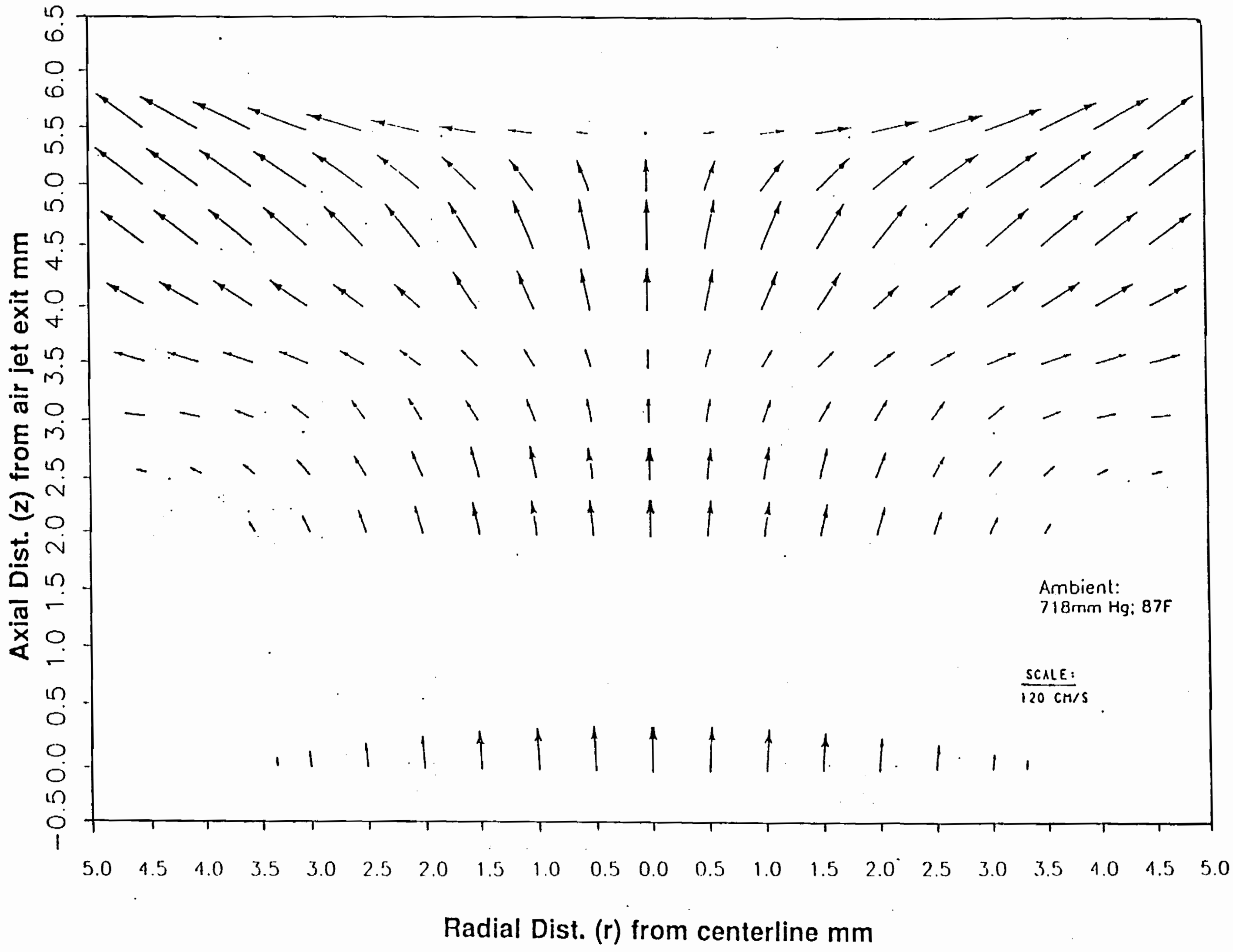

Figure 25 A velocity vector plot of the measured velocity @the higher strain rate case.

for both cases. Especially for the higher flow rate case, the vector plot (Fig.25) gives the impression of two stagnation regions of flow. That is, from the cold input the axial flow decelerates, but does not actually stagnate, as if it approaches a stagnation plane. This region of flow is termed the "pseudo-stagnation region".[28] This "pseudo-stagnation plane" (flame boundary)[5] is located at z=~3.50 mm for both cases. Also, near this plane, the flow for both cases appear to be converted to radial flow, especially near the jet radius. And it can be seen that approximately only the center portion of the flow goes through this plane, and is "processed" by the flame. After the "pseudo-stagnation plane", the flow is accelerated, as evidenced by the dramatic increase in velocities in excess of the jet exit velocity, by the energy released from the flame. As the flow approaches the SP, all the flow is converted to radial flow with no signs of any reversed or negative flow. From the lag modeling, particles of size greater than 5µm will penetrate the stagnation plane, and then be "pushed back" as negative reversed flow. From the "pseudo-stagnation plane" to the SP, the region of flow is commonly approximated as a "boundary layer region" by most modelers,[13,14,16,17] implying a thin reaction zone imbedded in a potential stagnation flow. During the velocity measurements for both cases, the data rates appeared to drop as the measurement volume approached the flame, and then dropped significantly after the flame by about two-thirds.

Greater quantitative details along the stagnation streamline are shown in Fig.26 and 27 where the lower and higher flow rate cases are plotted. Both cases exhibit the classical "N" shape axial velocity profile along the best estimated centerline of the OJB system. Slight misalignment of this centerline is evident by the small non-zero radial

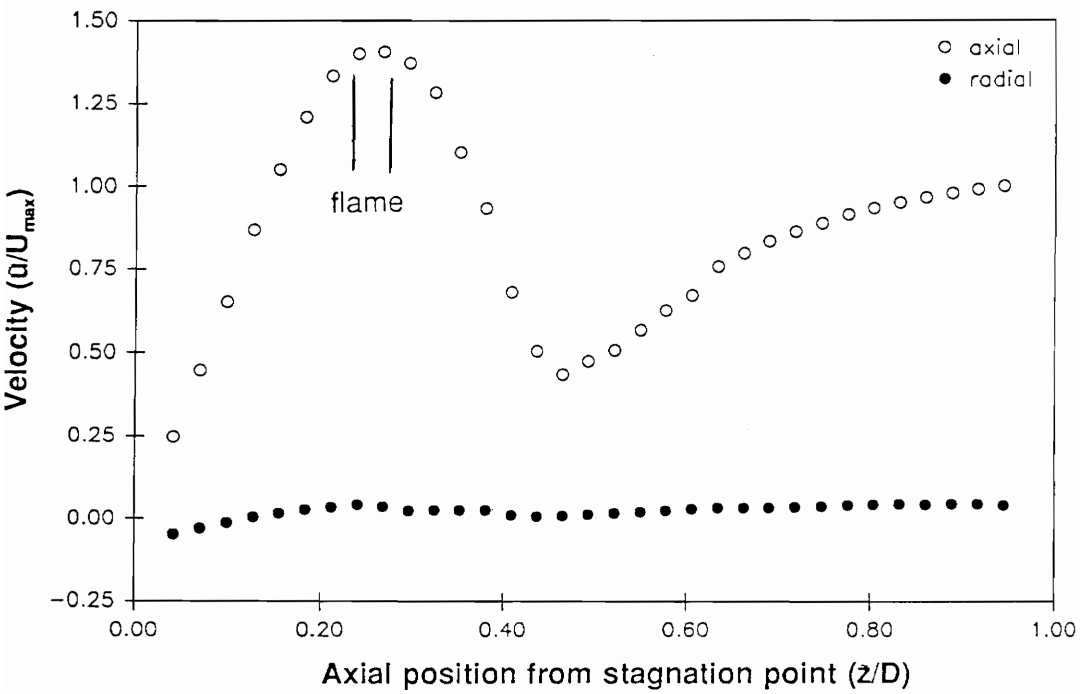

Figure 26 Velocity measurements along the stagnation streamline @the lower strain rate case

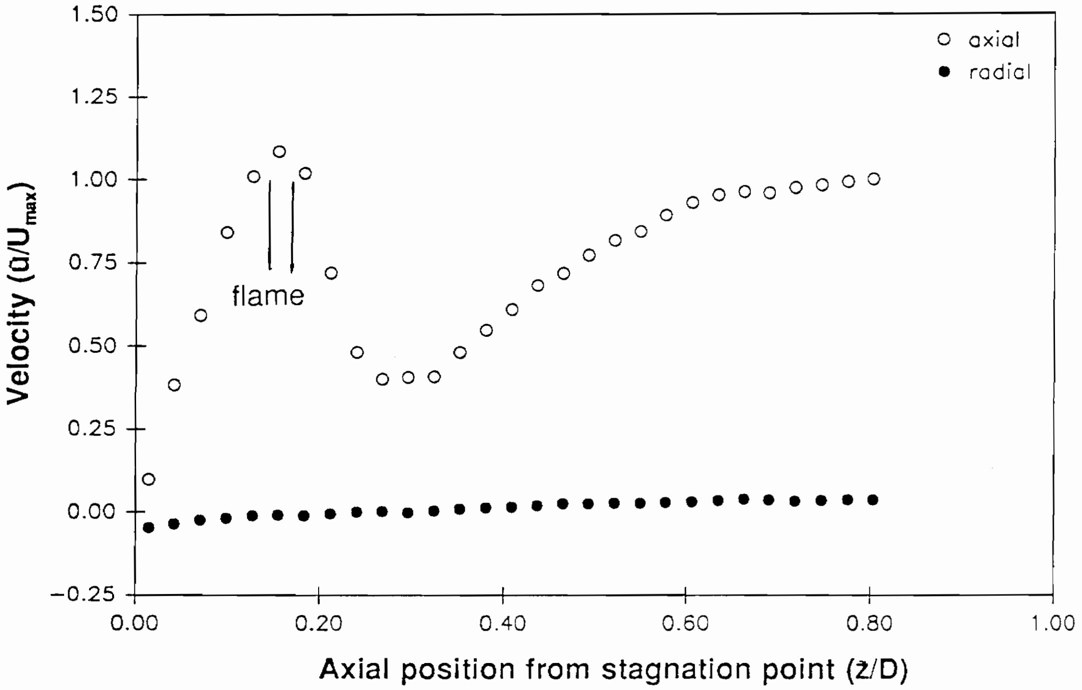

Figure 27 Velocity measurements along the stagnation streamline @the higher strain rate case

velocities. Several features in Fig.26 are observed: beginning from the air jet exit and consistent with the corresponding vector field plot, the axial velocity decreases as it approaches the flame zone; the axial velocity then attains a relative minimum before the flame (this corresponds to the "pseudo-stagnation plane") zone; in the flame zone, the axial velocity increases and reaches a maximum; finally, as the flow continues toward stagnation, the axial velocity falls to zero as it approaches the stagnation point. The same behaviour is observed in Fig.27 for the higher strain rate case.

In both cases, as the flow approaches the actual SP, the axial velocity increases almost linearly with distance from the stagnation plane. Furthermore, no negative axial velocities are measured. This is an indication of relatively small sized seeds with corresponding lower lag rates.

In the vicinity of the relative minimum, a "pseudo-stagnation point"[28] (flame boundary) is observed. As noted above, this "pseudo-stagnation plane" was clearly identified in the velocity vector field plotted, as shown in Fig 24. The same is true for the higher flow rates case, shown in Fig.25. In the flame region, the flow is heated up by the energy release from the reaction, and the flow accelerates. From the "pseudo-stagnation plane" to the downstream actual stagnation point, this entire region ("boundary layer region") appears relatively thick which is inconsistent with the approximation of most modelings.[13,14,16,17] Near the flame, the axial velocity reaches a maximum of approximately one and a half times the input axial velocity for the lower case, which corresponds to the highest temperature from Pellett[5] et al. CARS measurement of the temperature field. The higher flow case "boundary layer region" appears thinner than the lower flow rate case.

The following Fig.28-37 (for the lower flow rate case) show the radial distribution of axial (*u*) and corresponding radial (*v*) components for several axial positions relative to the air jet exit. The axial position (*z*) are 0.00, 2.50, 3.00, 3.50, 4.00, 4.50, 5.00, 5.50, 6.00 and 6.50 mm. For the higher flow rate (Fig.38-46) the axial position (*z*) are 0.00, 2.00, 2.50, 3.00, 3.50, 4.00, 4.50, 5.00, 5.50 mm.

From Fig.28-37, a few general observations can be made. Except for Fig.28 (which is at the jet exit), the radial velocity, *v*, behaves linearly with *r* near the centerline for all axial locations. The axial velocity, *u*, distribution varies with *r*. That is, it is not uniform as assumed in both current modeling techniques. However, *u* is approximately uniform in *r* at *z*=3.5 mm, Fig.31, which is near the "pseudo-SP". Also at this particular axial location, the radial velocity, *v*, is linear in *r*. At this particular axial location, the velocity components approximate the "traditional" modeling boundary conditions exactly, although this location is very close to the flame.

Similar observations can be made for the higher strain rate case (Fig.38-46).

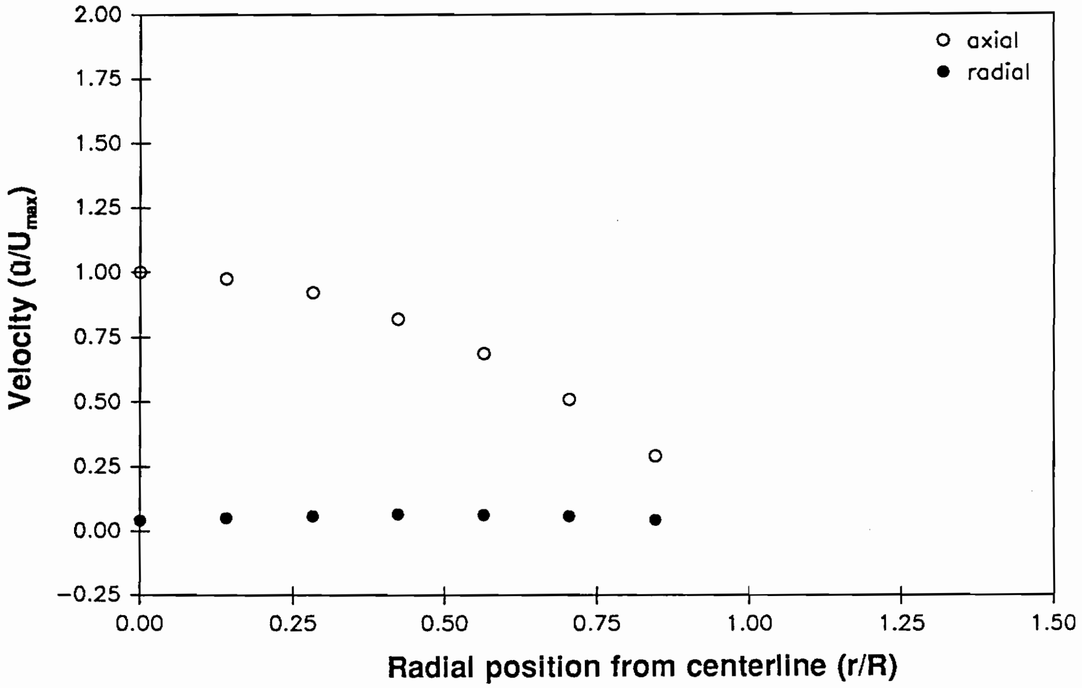

Figure 28 Velocity measurements along the axial plane z=0.00 mm @the lower strain rate case

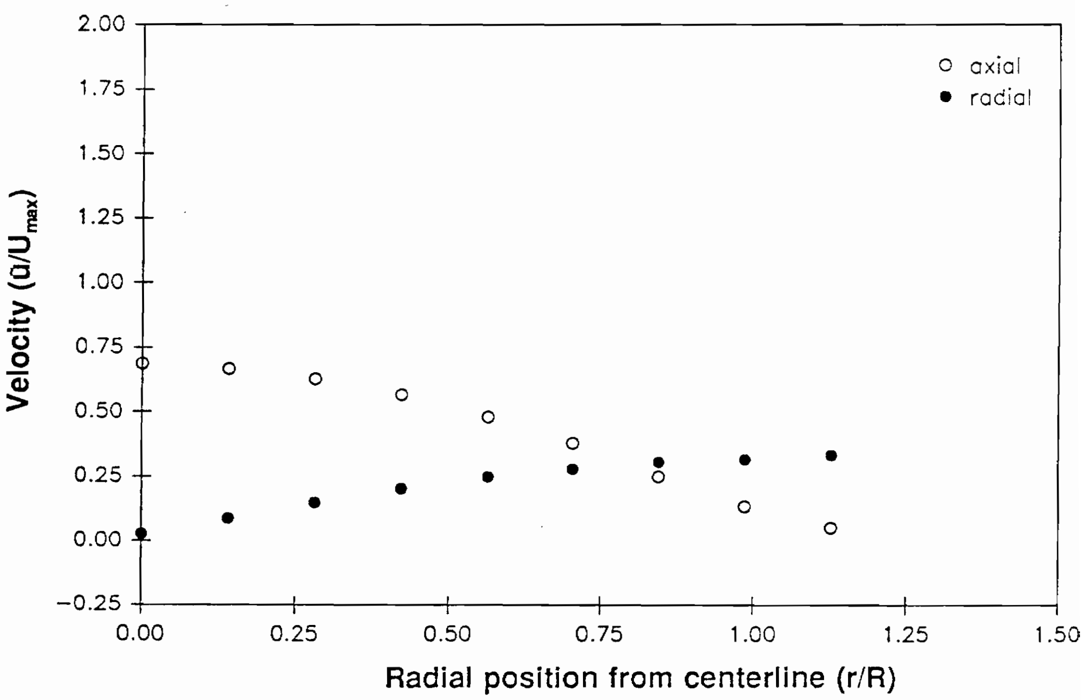

Figure 29 Velocity measurements along the axial plane z=2.50 mm @the lower strain rate case

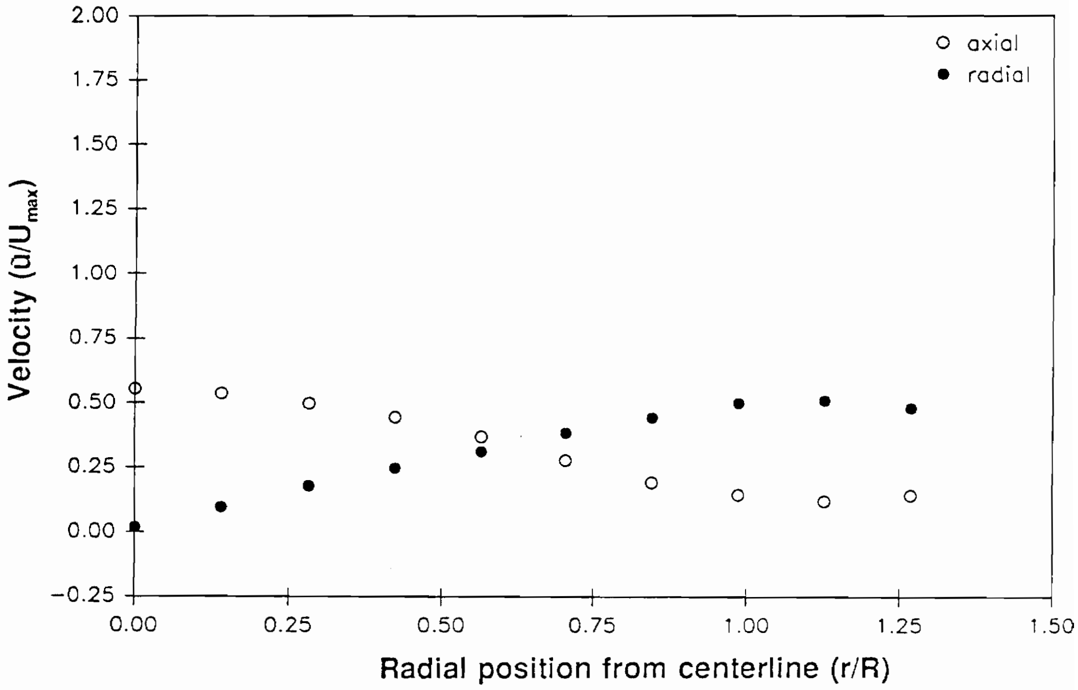

Figure 30 Velocity measurements along the axial plane z=3.00 mm @the lower strain rate case

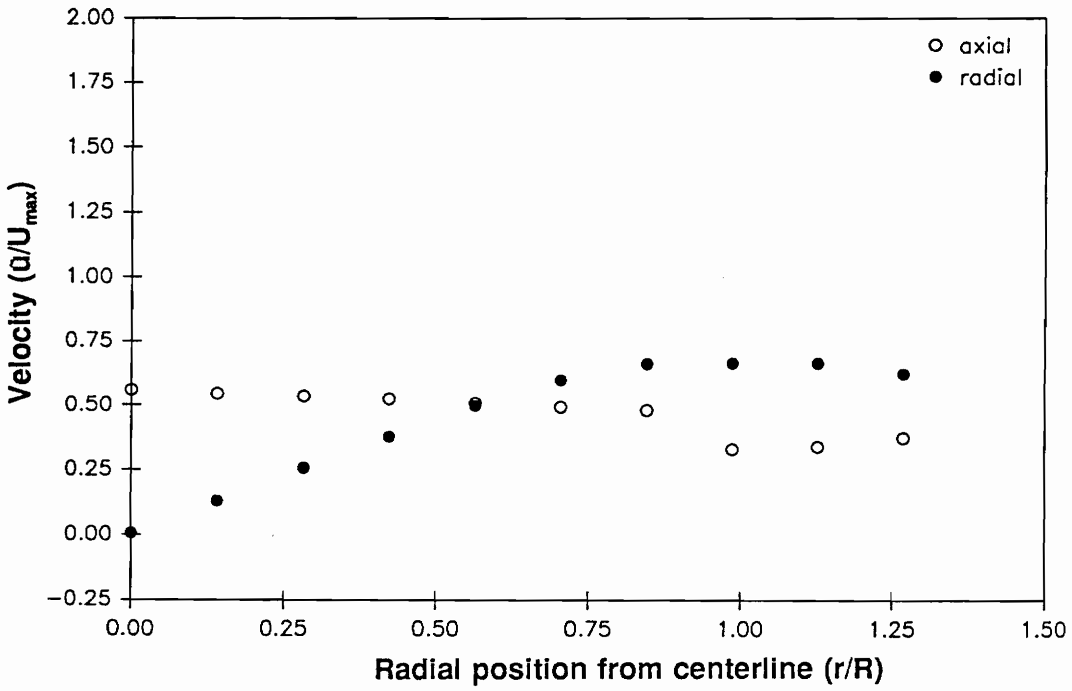

Figure 31 Velocity measurements along the axial plane z=3.50 mm @the lower strain rate case

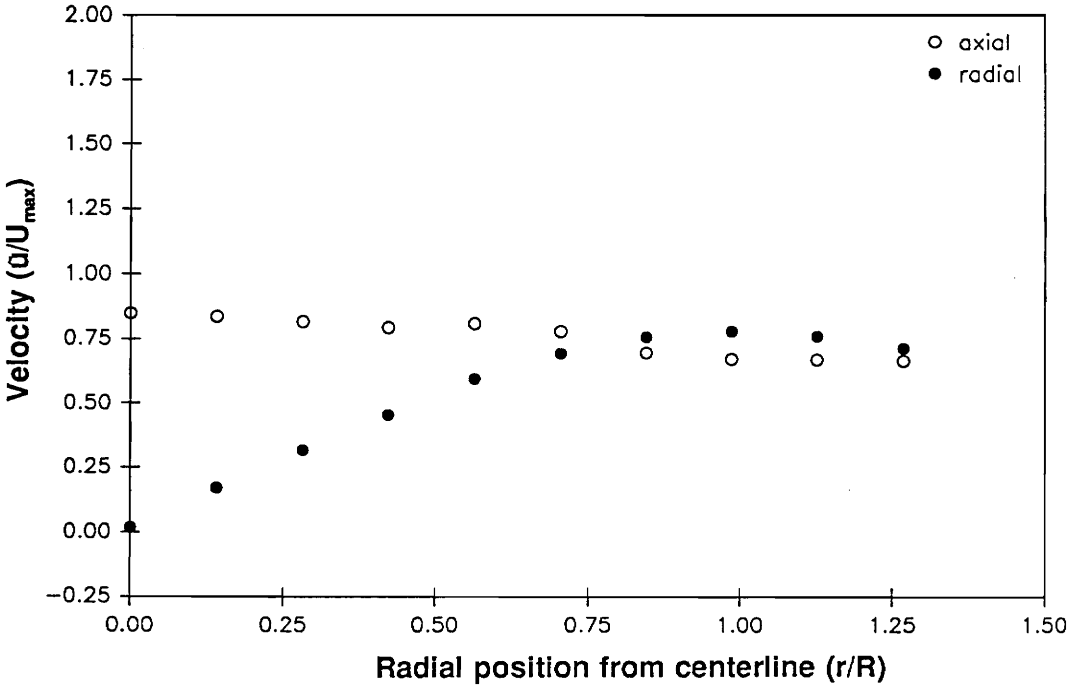

Figure 32 Velocity measurements along the axial plane z=4.00 mm @the lower strain rate case

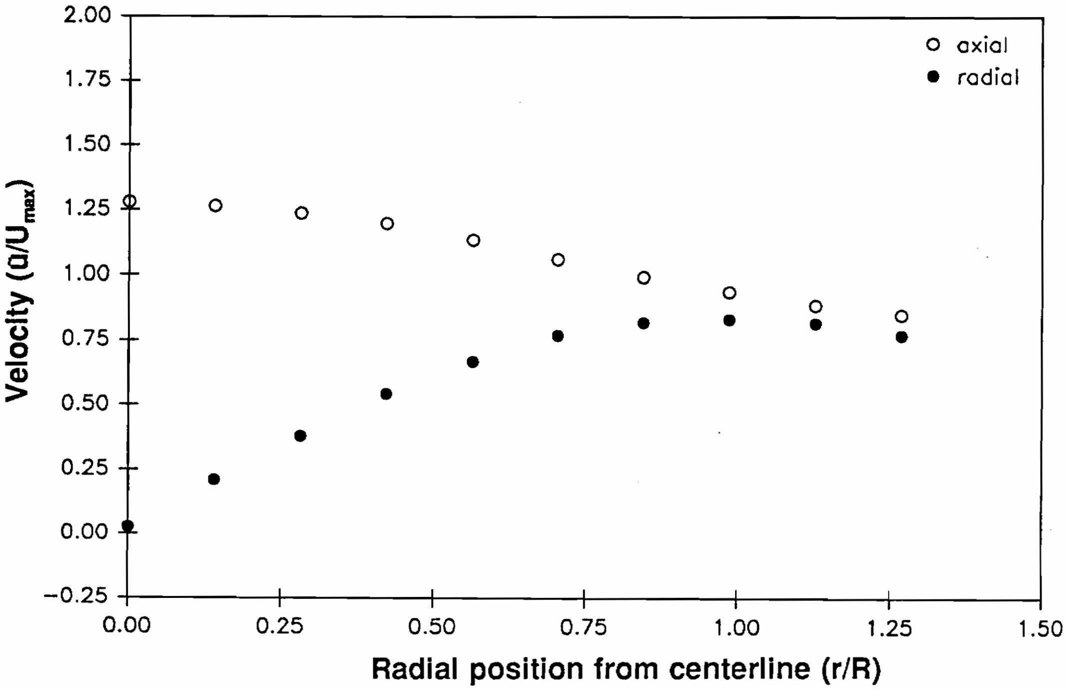

Figure 33 Velocity measurements along the axial plane z=4.50 mm @the lower strain rate case

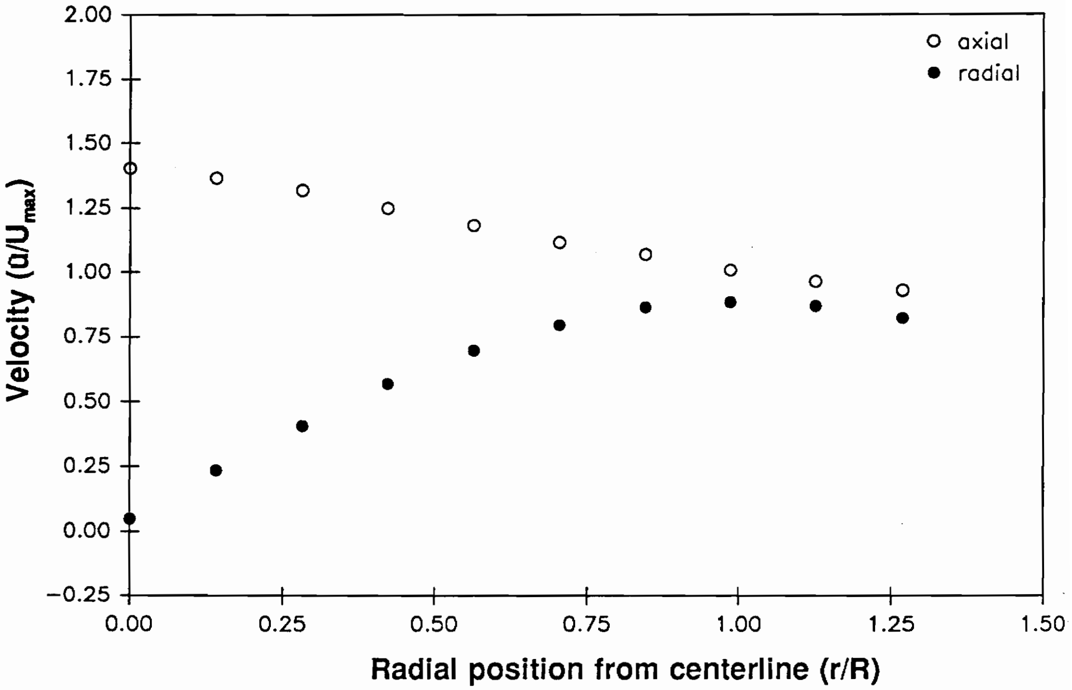

Figure 34 Velocity measurements along the axial plane z=5.00 mm @the lower strain rate case

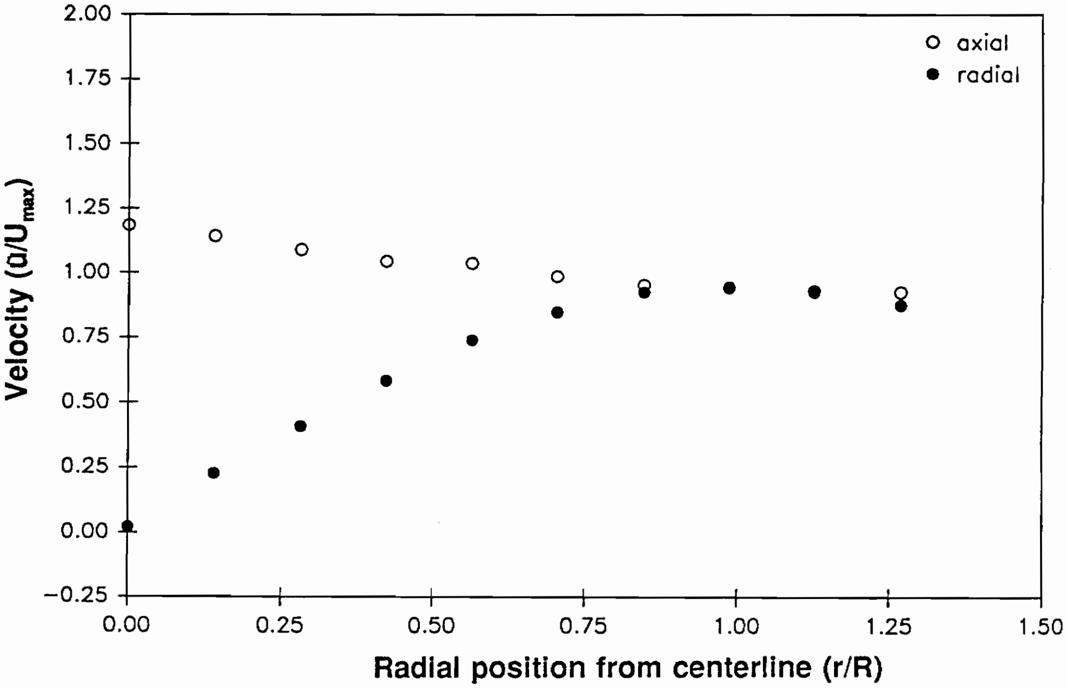

Figure 35 Velocity measurements along the axial plane z=5.50 mm @the lower strain rate case

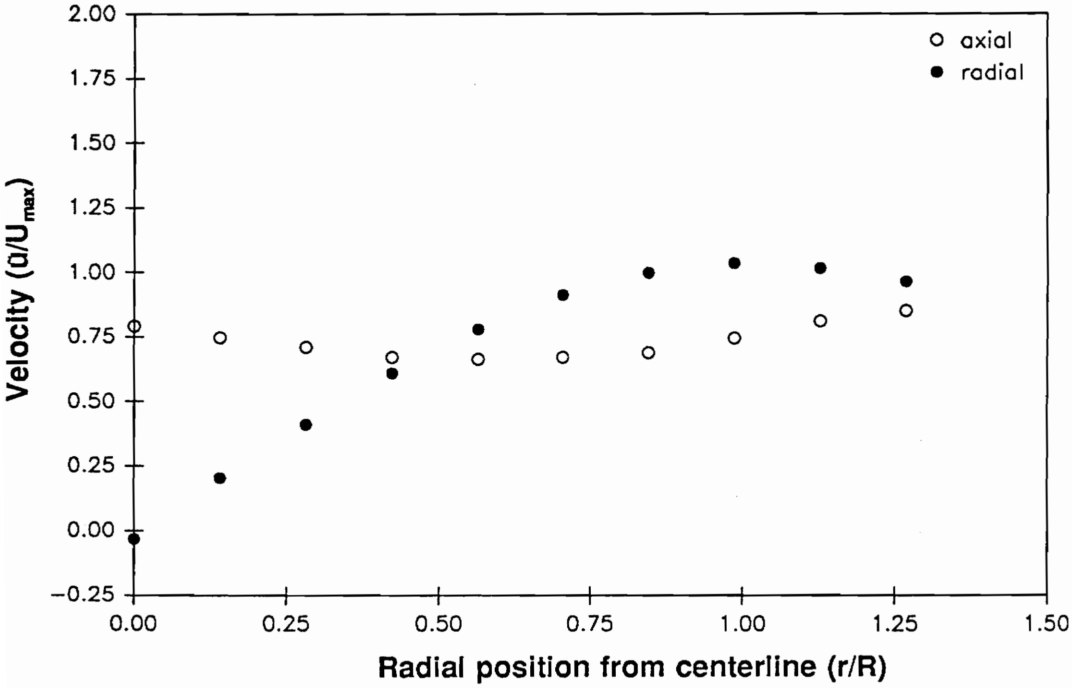

Figure 36 Velocity measurements along the axial plane z=6.00 mm @the lower strain rate case

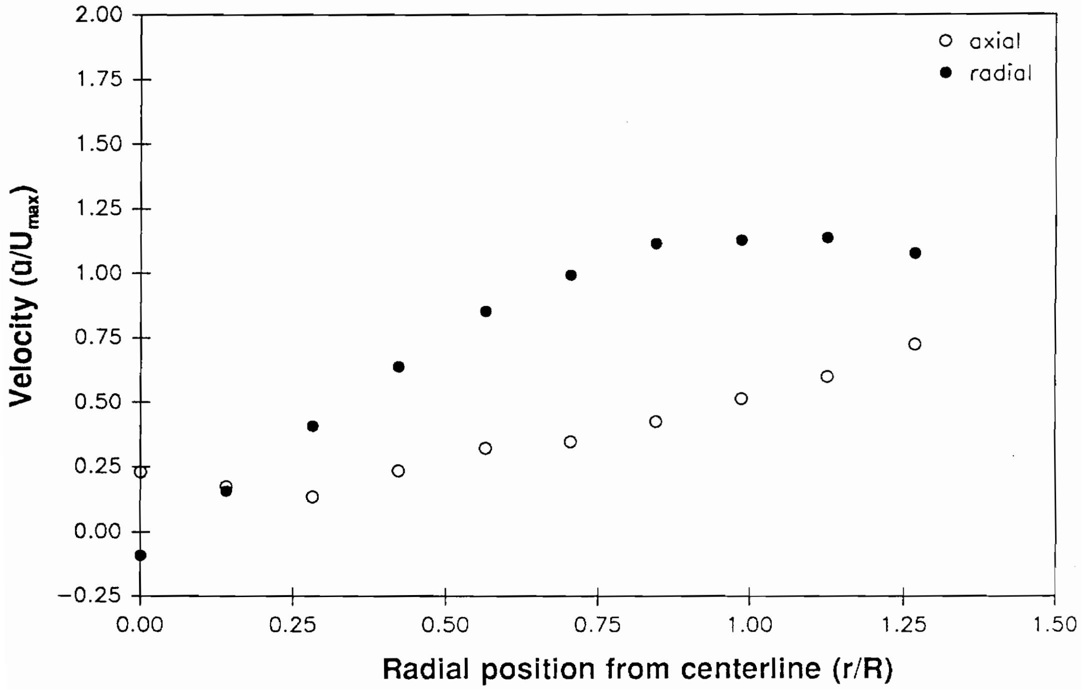

Figure 37 Velocity measurements along the axial plane z=6.50 mm @the lower strain rate case

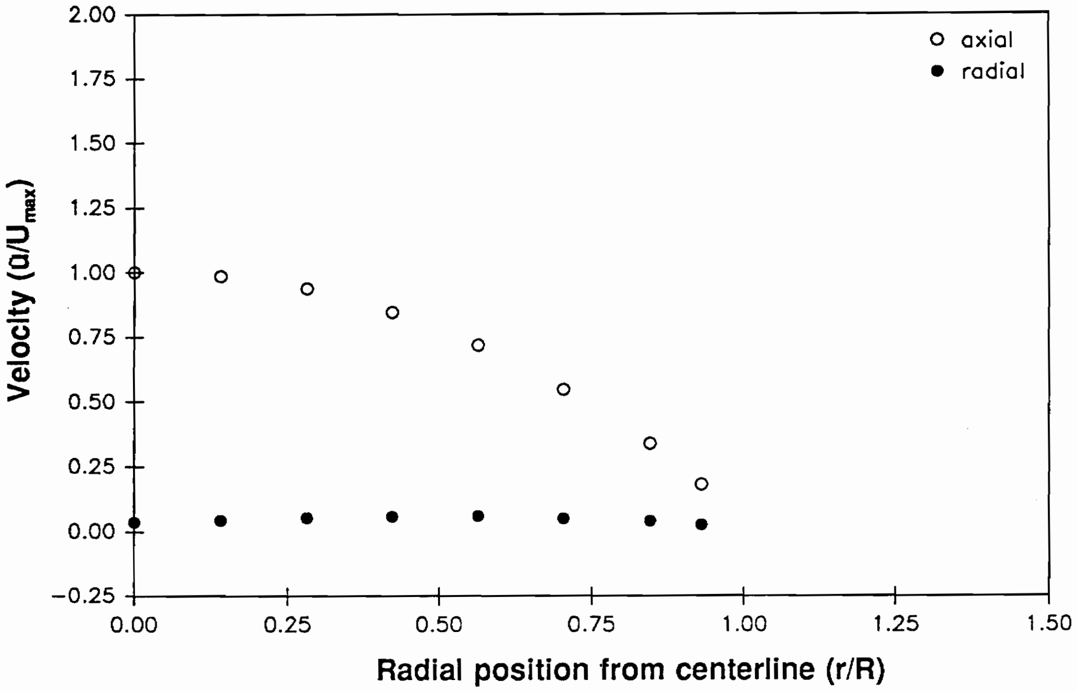

Figure 38 Velocity measurements along the axial plane z=0.00 mm @the higher strain rate case

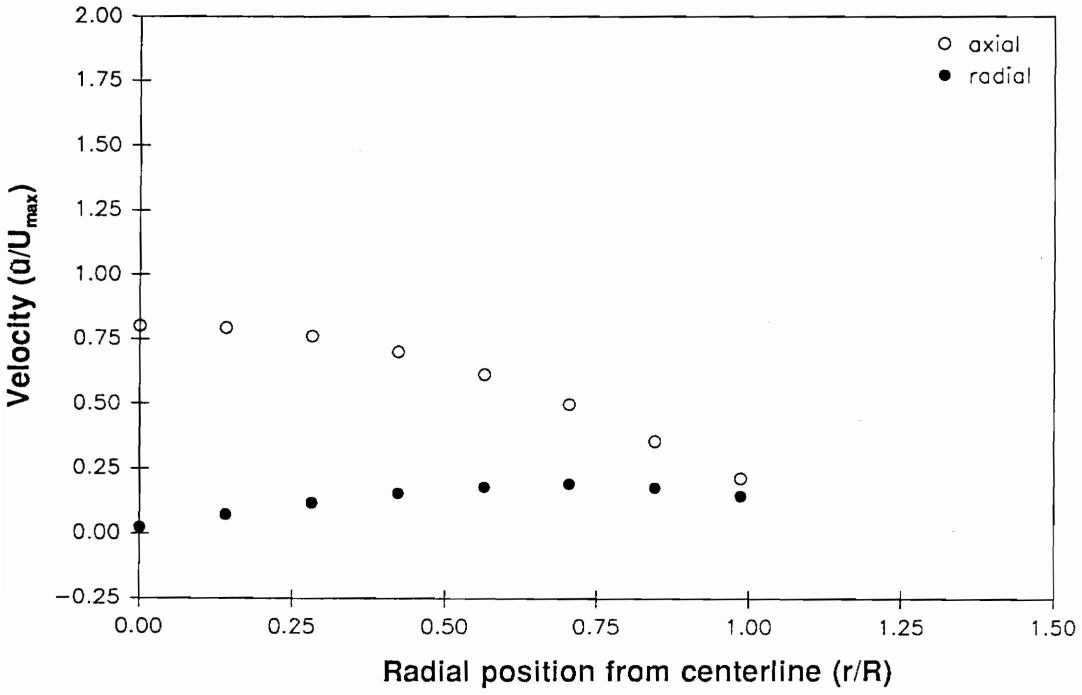

Figure 39 Velocity measurements along the axial plane z=2.00 mm @the higher strain rate case

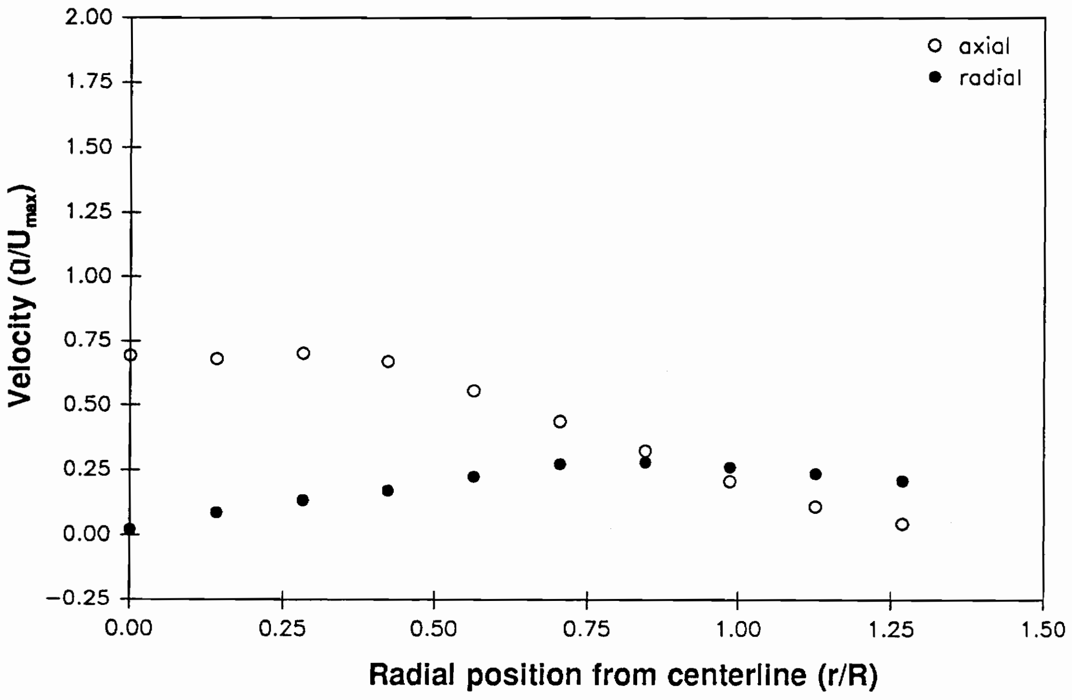

Figure 40 Velocity measurements along the axial plane z=2.50 mm @the higher strain rate case

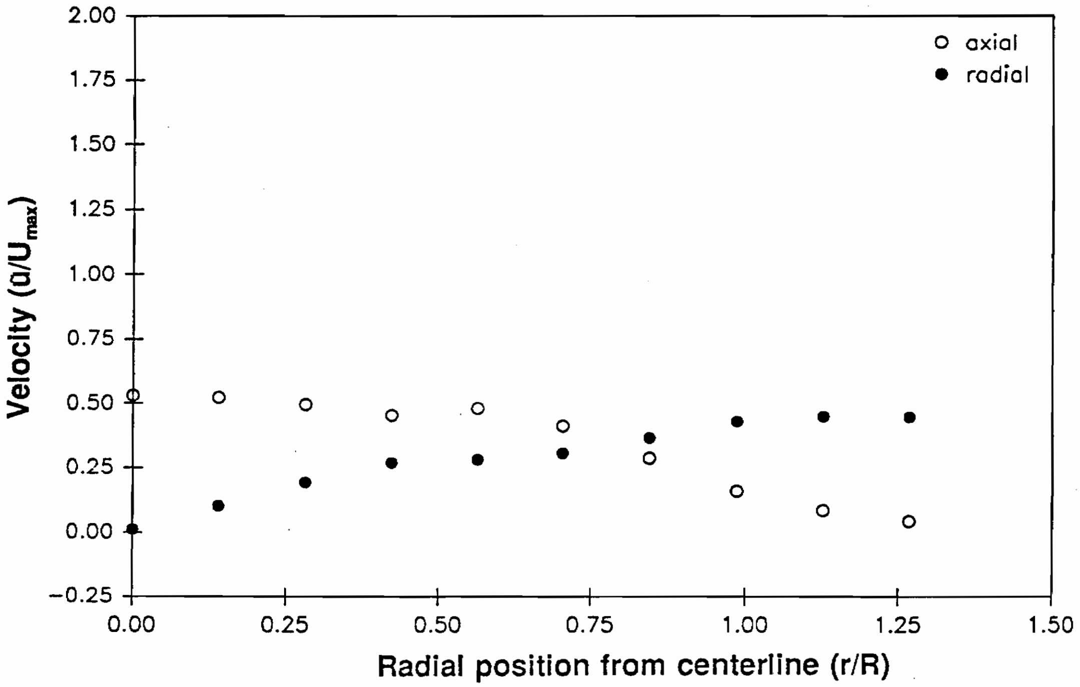

Figure 41 Velocity measurements along the axial plane z=3.00 mm @the higher strain rate case

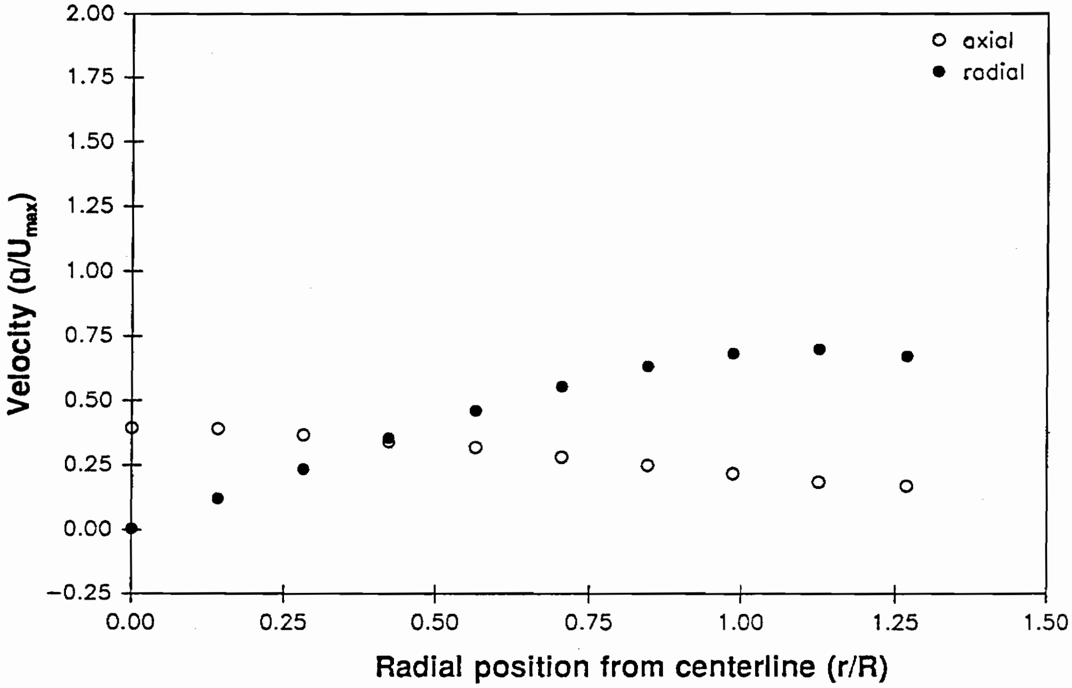

Figure 42 Velocity measurements along the axial plane z=3.50 mm @the higher strain rate case

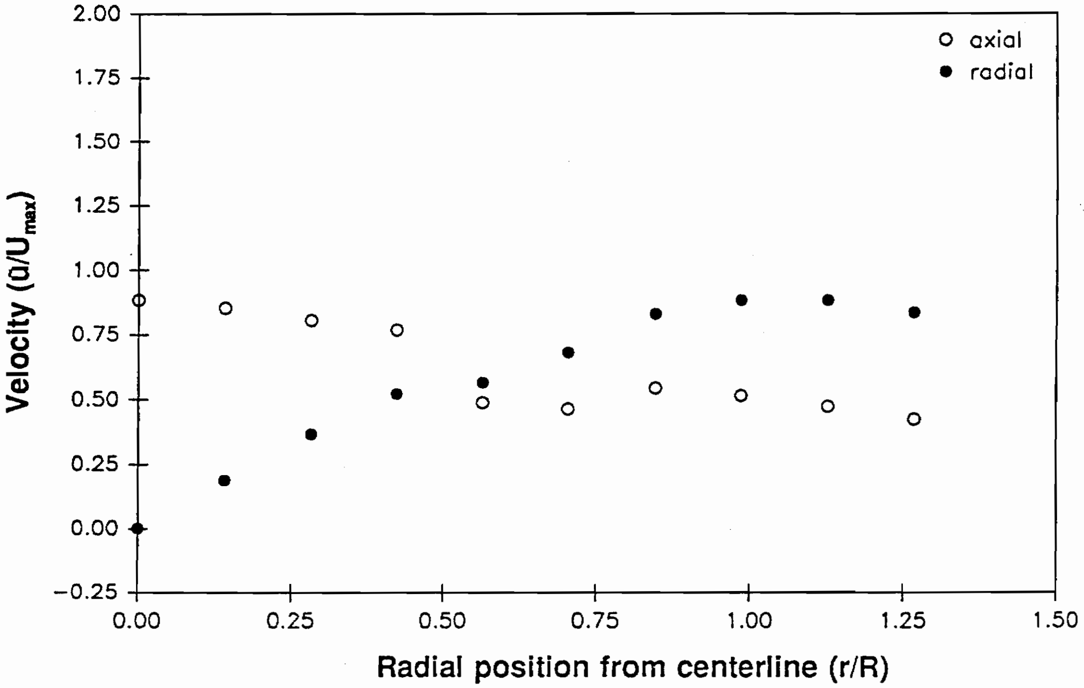

Figure 43 Velocity measurements along the axial plane z=4.00 mm @the higher strain rate case

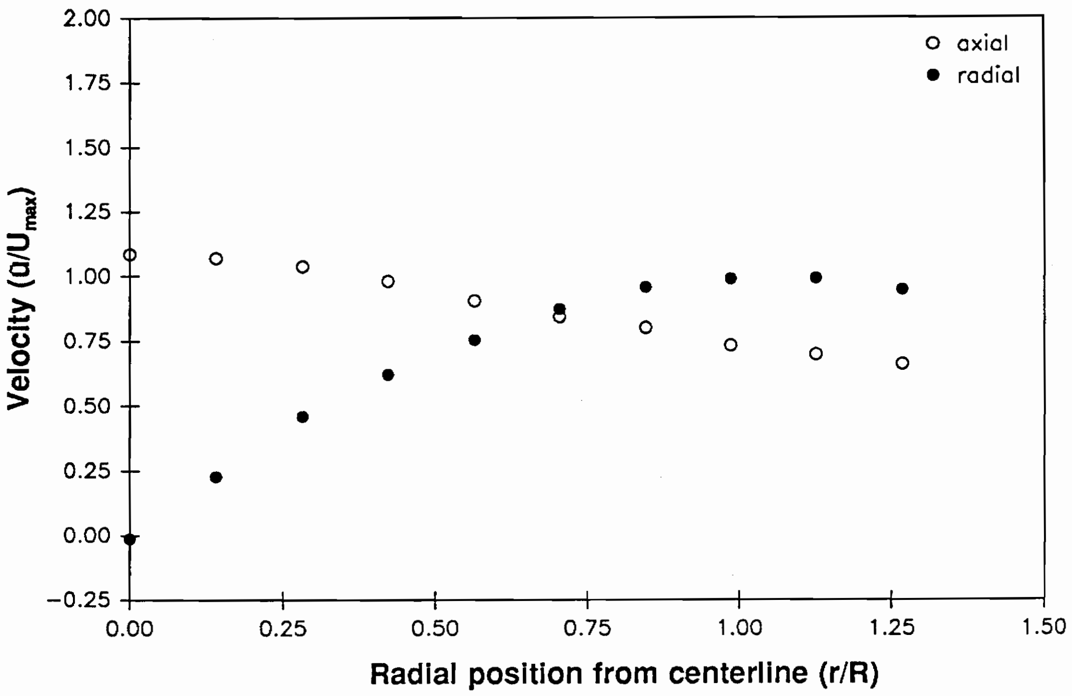

Figure 44 Velocity measurements along the axial plane z=4.50 mm @the higher strain rate case

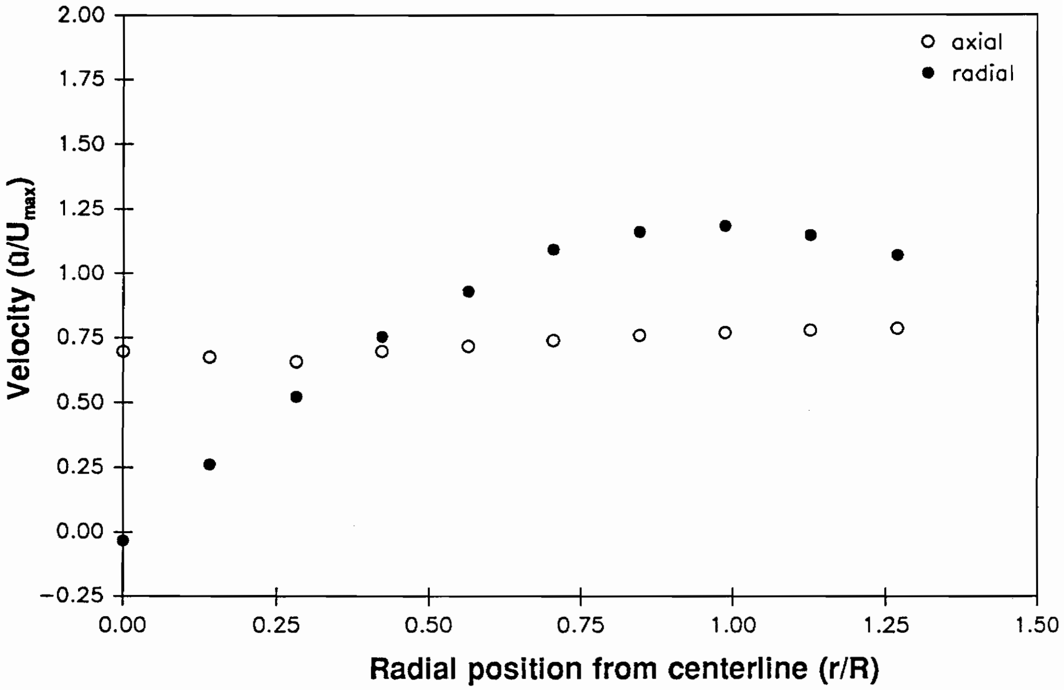

Figure 45 Velocity measurements along the axial plane z=5.00 mm @the higher strain rate case

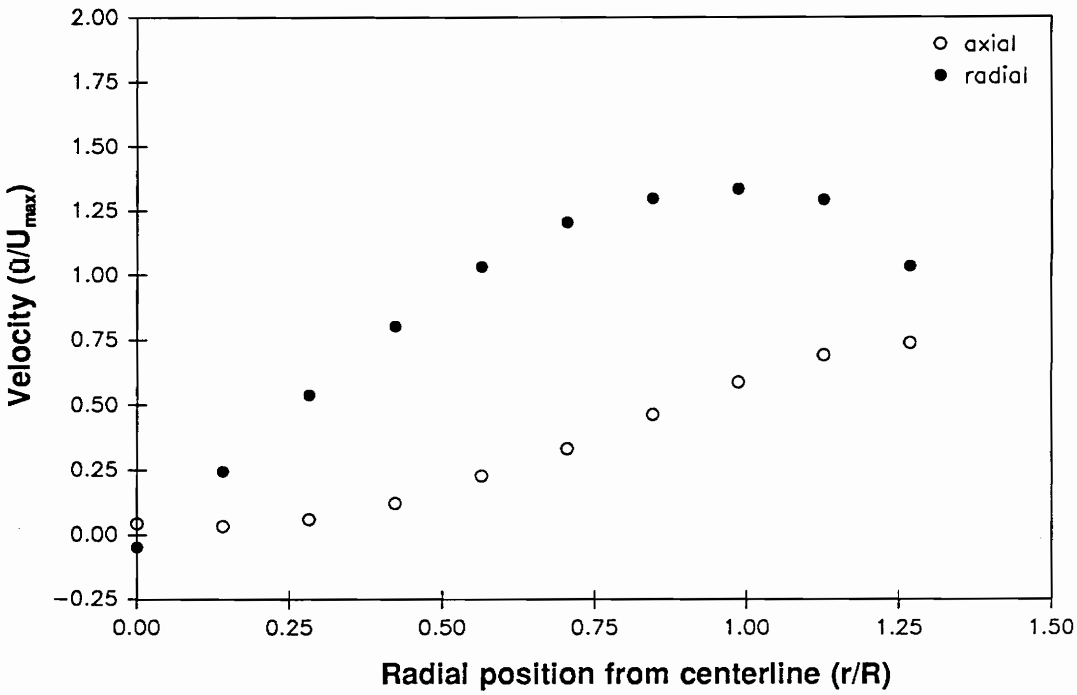

Figure 46 Velocity measurements along the axial plane z=5.50 mm @the higher strain rate case

3.3 Comparisons with published models

One of the first goals in this research was to reproduce the classical "N" shape centerline velocity profile reported. These "N" shape or stagnation streamline velocity profiles as shown in Fig.26 and 27, are in good agreement with CARS profiles of the temperature field (Fig.51)[5] in a similar CFDF flow field, and qualitatively agree with model predictions[13,14,16,17,19] and other experimental results.[5,6,9-12,19] The maximum temperature locations correspond to the maximum axial velocities observed. Upstream of the flame boundary, the temperature field is nearly uniform near ambient temperature[5,6], and the velocity flow field behaves as it would in a cold stagnating flow.

In the "traditional" modeling of the CFDF[13,14,16], a single parameter is used to characterize the flow field. This single parameter is the strain rate of the assumed free potential flow. By approximating the flow as a stagnation-point potential flow (Hiemenz flow) with a boundary layer superimposed[2], the freestream velocity field is easily quantified, that is, $u=-2az$ and $v=ar$, where u is the axial (z) velocity; v is the radial (r) velocity, and a is the specified potential-flow velocity gradient. That is, this specified constant gradient a is applied and imposed at the freestream until the flame-induced strain rate variation takes effect near the "pseudo-SP". The specified strain rate is used in this model as the determining parameter in the flame region, and it is assumed this parameter will determine the flame extinction. Also, this model assumes that the flow is irrotational, that is,

$$-\frac{1}{2}\frac{\partial u}{\partial z} = \frac{\partial v}{\partial r} = a \tag{2}$$

This irrotational assumption can be tested experimentally, by computing $-(\partial u/\partial z)/2$ and $\partial v/\partial r$ from the velocity component data as shown in Fig.47. From Fig.47, the axial velocity does not vary linearly with the axial position *z* from the air jet exit to the "pseudo-SP". That is, $\partial u/\partial z$ is not constant within this "pseudo-SP region". Also, from Fig.26 it is observed that the axial velocity does not vary linearly with *z*. This is at variance with this modeling assumption which assumes a potential freestream flow. However, just upstream of the "pseudo-SP" the above irrotational assumption (Eq.1) appears to be satisfied. At this location, the strain rate is approximately equal to the supply air strain rate a_{input}, that is, $a/a_{input} = 1$. This a_{input} is defined as the ratio of U_{max} to the jet diameter D.[5] Also at this location (which corresponds to Fig.31 from the previous section), the axial and radial velocity distributions approximate the boundary conditions appropriate to the "traditional" model exactly.

Past the "pseudo-SP", Fig.47 shows that there are large variations in $-(\partial u/\partial z)/2$ in the "boundary layer region" (flame zone), which illustrate the large effect of heat release on the straining field. However, $(\partial v/\partial r)$ is monotonically increasing toward the true SP, with the largest magnitude at SP of approximately three and a half times that at the "pseudo-SP". Within the flame zone, Fig.26 shows that *u* goes through a maximum near the maximum temperature point (from corresponding CARS data)[5,6], that is $\partial u/\partial z = 0$ at the maximum point. However, Fig.47 shows that at $-(\partial u/\partial z)/2 = 0$, $(\partial v/\partial r)$ is not zero, and is approximately two and a half times of a_{input}. This indicates that there is a large radial stretching of the flame zone, even when the axial strain is zero. Figures 27 and 48 show qualitatively the same conclusions at the higher a_{input}.

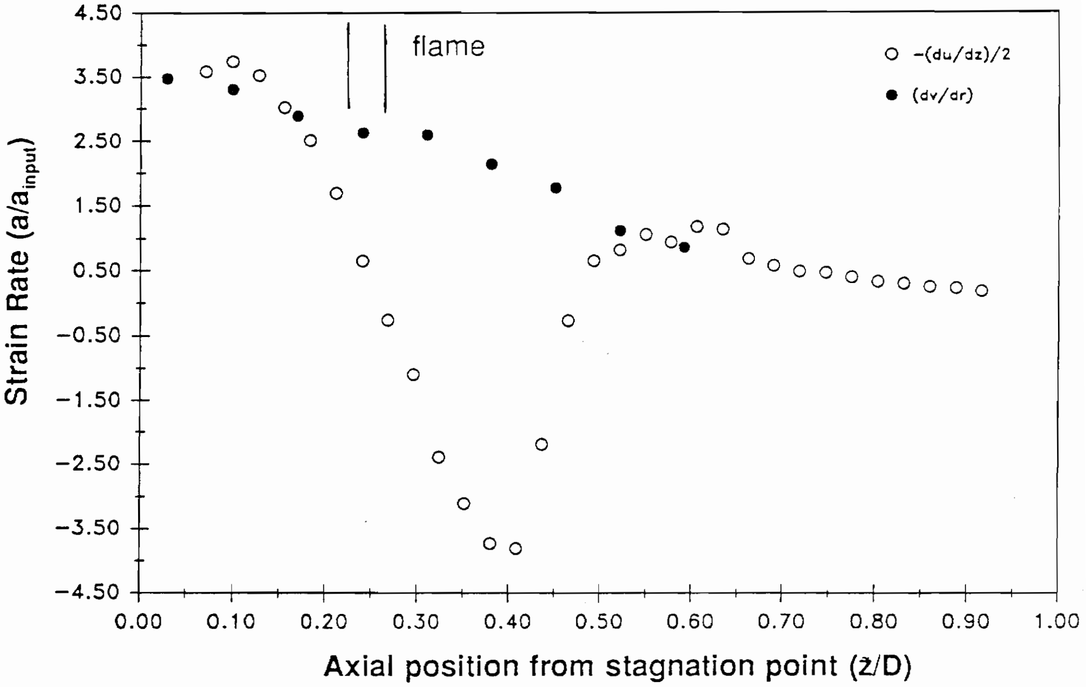

Figure 47 Computed axial and radial strain rate along stagnation streamline @the lower strain rate case

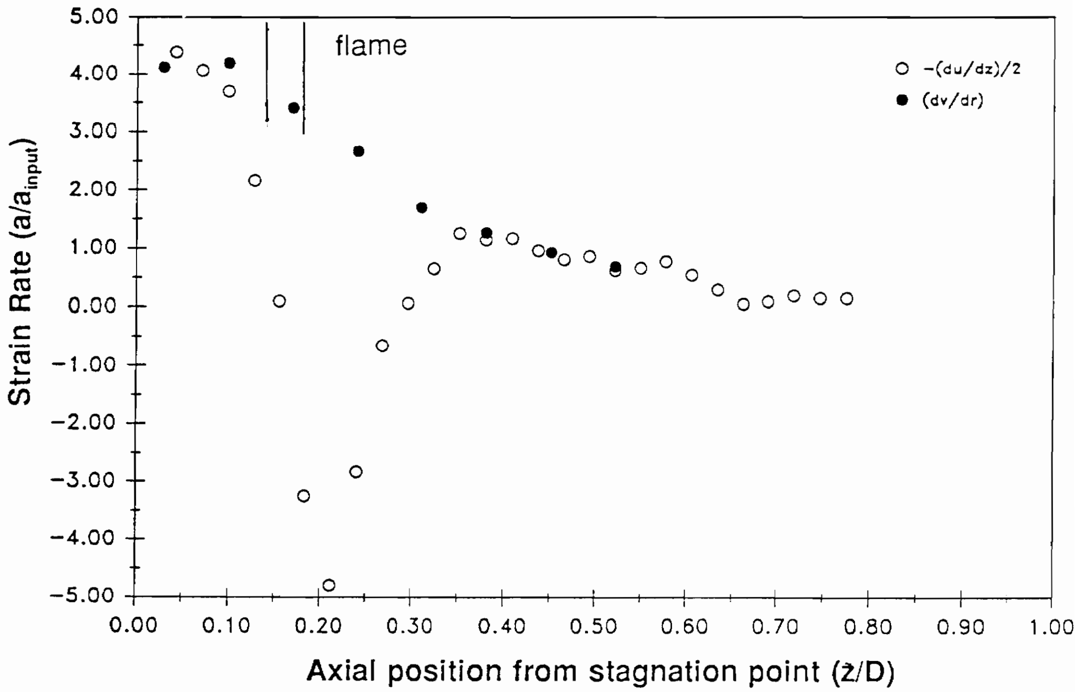

Figure 48 Computed axial and radial strain rate along stagnation streamline @the higher strain rate case

In another modeling of CFDF introduced by Kee et al.,[17] a defined streamfunction [$\psi(z,r) = r^2 U$, where $U{:}U(z)$] is found to satisfy the mass continuity equation:

$$\frac{\partial}{\partial z}(r\rho u) + \frac{\partial}{\partial r}(r\rho v) = 0 \tag{3}$$

if the streamfunction is defined such that:

$$\rho v = -r\frac{dU}{dz} \tag{4}$$

$$\rho u = 2U \tag{5}$$

Here u and v are the axial (z) and radial (r) velocity components respectively. It is further assumed that: temperature, species mass fraction, and density are functions of axial position z only. Since the density is assumed to be function of z only, Eq.4 implies that the radial velocity at each axial plane, varies linearly with r. From the previous section, the measured radial velocity does vary almost linearly, to a good approximation, with the radial distance (r), from the centerline to approximately the tube radius at each different axial position in the flow field (Fig.29-37 for the lower flow case, Fig.39-46 for the higher flow case), that is, the modeling assumption is verified in these experiments. In this model, Kee et al.[17] does not specified any characteristic strain rate, but it allows the model to calculate the strain rate field in the course of the solution. However, Kee et al. does specify a freestream velocity distribution, that of a plug flow (that is, there is no radial component of the velocity).

Similarly, this model approximation can be tested by taking the ratio of the last two equations (Eq.4 & 5), so the density is eliminated. The following equation is obtained:

$$\frac{v}{u \cdot r} = -\frac{dU/dz}{2U} \qquad (6)$$

Since *U* is defined, *U*:*U*(*z*), as a function of *z* only, the right-hand side of the above equation (Eq.5) can only be a function of *z*. The left-hand side of the equation, which can be computed from the velocity measurements, should collapse to a single function of *z* if the modeling approximation is correct. Figure 49 is a plot of this parameter for all measured data, plotted as a function of the axial position *z*, for the lower strain rate case. It is noted from this plot that for *r* less than or equal to the tube radius, the data does collapse satisfactorily, indicating that the functional form [$\psi(z,r)$] assumed is justified within this region. However, the data does not collapse well near the stagnation point. Similarly, the same can be said for the higher flow rates case, as shown in Fig.50.

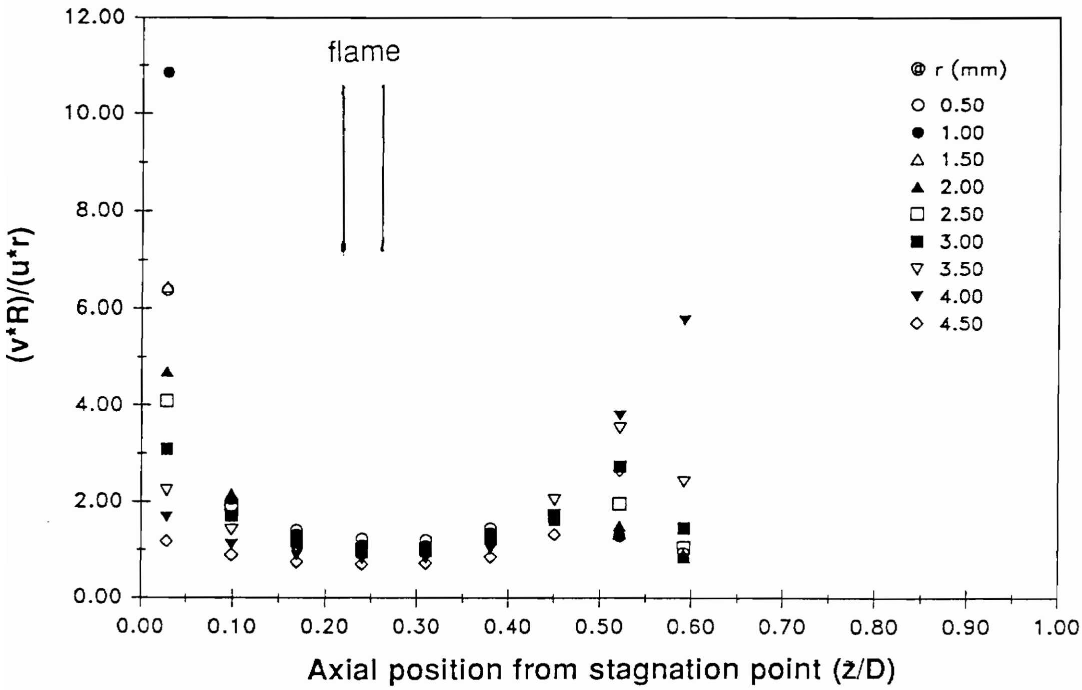

Figure 49 Plot of the lower flow rate case based upon Kee's model

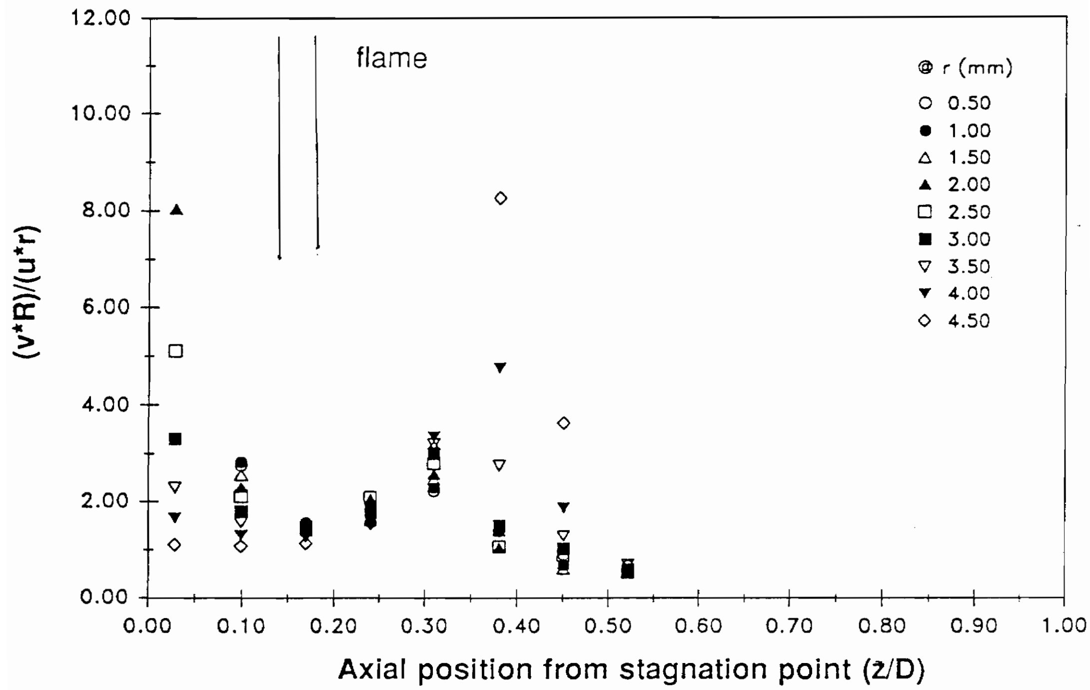

Figure 50 Plot of the higher flow rate case based upon Kee's model

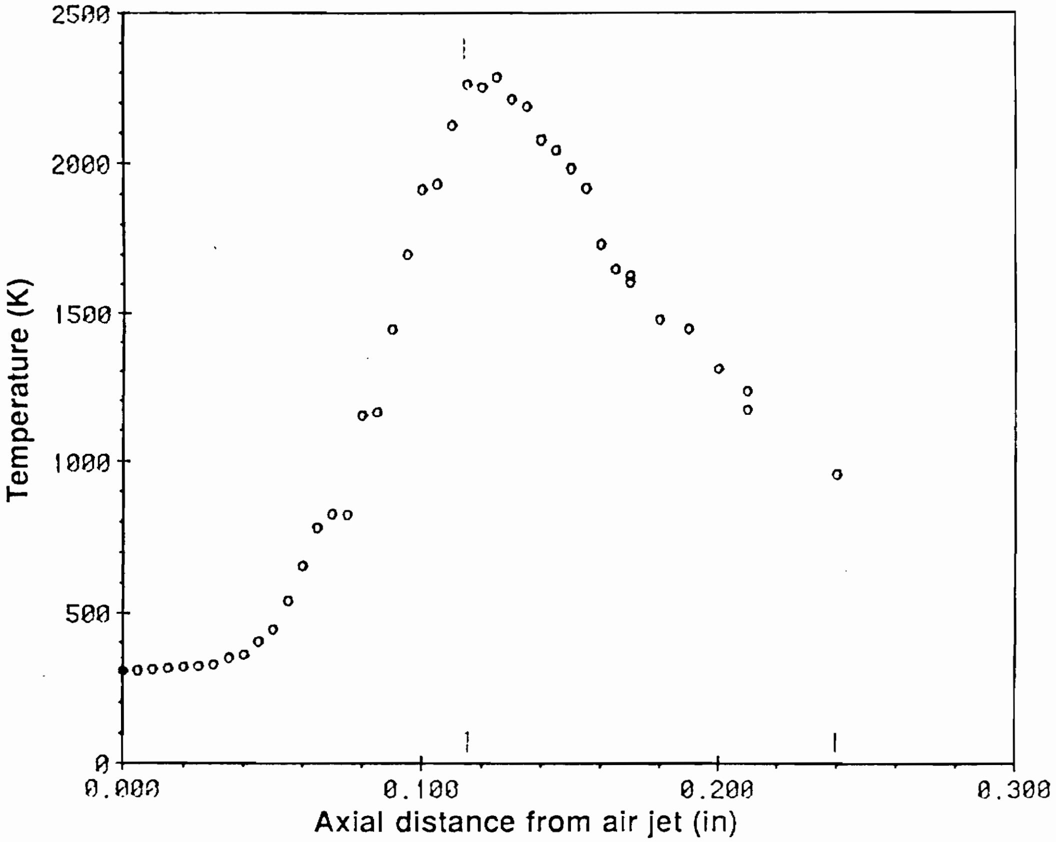

Figure 51 Temperature profile along stagnation streamline @the lower strain rate conditions

In summary, the data (for both flow cases) shows that the radial velocity is approximately linear with radial coordinate. The boundary conditions (uniform u, and linear *v* in *r* direction) assumed by the "traditional" model are appropriate at a particular location upstream of the boundary layer, within the flow. The supply air strain rate a_{input} appears to approximate the potential flow strain rate, going into the flame zone. Qualitatively, Kee's model appears to approximate the velocity distribution over the entire region of flow better, for both flow cases,[28] despite the fact that the supply air velocity profile is parabolic rather than uniform, as assumed by Kee et al.

4. CONCLUSIONS AND RECOMMENDATIONS

The LDA velocity measurements clearly show that the H_2-Air flame is on the air side of the flow field as predicted by earlier investigators. From the limited data presented, several of the prevailing assumptions and approximations used by CFDF modelers were investigated. That is, the data shows that the radial velocity is approximately linear in the radial coordinate, as assumed by most models; the boundary conditions (uniform axial velocity, and linear radial velocity) assumed by the "traditional" model are appropriate at a particular location upstream of the boundary layer region; the supply air strain rate approximates the potential flow strain rate at least at a point just upstream of the flame zone; however, the strain rate profile and axial velocity profile along the stagnation streamline are more characteristic of the plug flow model introduced by Kee et al. The boundary layer region, however, appears relatively thicker than implied by the "traditional" model, for both flow cases. However, the two flow rate cases investigated were below the flame extinction limit, and the models predictions of extinction conditions are less than satisfactory on experiments reported thus far. Extensive data may be required on both the air side and the fuel side at much higher flow rates, especially towards extinction limit, before the accuracies of the assumptions and approximations can be fully assessed.

It has been shown that the essential features of a CFDF hydrogen-air diffusion flame structure can be obtained accurately with this fairly simple OJB arrangement. The data obtained at these two strain rates are highly reproducible. In all, this OJB arrangement together with LDA system is useful in studying the fluid mechanics of CFDF structure.

It is recommended that velocity measurements be made at strain rates approaching extinction. In fact, measurements were attempted at flow rates much higher than those reported (that is, at nitrogen flow rates of 1.00 and 1.50 slpm), but the flame motions were too erratic and not reproducible enough to make a complete axial sweep on the centerline. One of the main problems appears to be an unsteadiness in the flow caused by the seeder at those flow rates. As the time required to make a complete axial sweep (not to mention a vector field mapping) is quite long, any the measurements would be compromised if the flame wandered during this time. Also larger particles were observed at these higher flow rates, indicating potential particle lag problems at these flow rates.

Because of the low pressures used in this experiment, the seeder was modified in order to seed the flow, hence the full potential of the seeder was not utilized. One suggestion that was implemented and proved successful was to have a larger settling chamber in the seeder. Seed samples collected have shown that smaller sized particles can be obtained with this larger chamber. This larger chamber helps to settle-out those big particles that would otherwise be entrained by the flow. Also, this large tank can act as a reservoir to reduce any unsteadiness from the seeder. This approach should improve the flame stability, so that measurements via LDA at higher strain rates can be attempted.

The present LDA system proved that accurate measurements can be obtained with such an instrument, despite the long acquisition time required. Alternative laser-based methods of velocity measurement should be explored (such as laser speckle, particle image velocimetry, etc), so that study at much higher strain rates (especially toward extinction limit) can be made in order to fully assess the potential of the modeling approximations presented. Also, the location of a_{input}, near the "pseudo-SP", should be tested to determine whether it is flow field dependent. And whether the flow field's observations, thus far, are geometry dependent (tube diameter, tube spacing,etc).

REFERENCE

1. Kuo,K.K. : Principles of Combustion, John Wiley & Sons, New York, 1986.

2. Dixon-Lewis,G. : Structure of Laminar Flames, Presented at Twenty-Third (International) Symposium on Combustion, 1990.

3. Peters,N. : Laminar Diffusion Flamelet Models in Non-premixed Turbulent Combustion, Prog. Energy Combust. Sci., pp.319-339, 1984.

4. Peters,N. : Laminar Flamelet Concepts in Turbulent Combustion, Twenty-First (International) Symposium on Combustion, pp.1231-1250, 1986.

5. Pellett, G.L., Northam,G.B., Wilson,L.G., Jarrett,O.Jr., Antcliff,R.R., Dancey,C.L., and Wang, J.A. : Opposed Jet Diffusion Flames of Nitrogen-Diluted Hydrogen vs Air; LDA and CARS Surveys; Fuel/Air Strain Rates at Extinction. AIAA Reprint AIAA-89-2522, July 1989.

6. Pellett,G.L., Guerra,R., Wilson,L.G., Jarrett,O.Jr., Antcliff,R.R., and Northam,G.B. : Blowoff, Restoration of Hydrogen-Air Opposed Jet Diffusion Flames; Effects of Air Contaminants and Fuel Additives; CARS Temperatures. Twenty-Second (International) Symposium on Combustion, 1988.

7. Guerra,R. : Effects of NO, CO, CO_2, and N_2 Air-Contaminants on Hydrogen-Air Diffusion Flames, M.S. Thesis, George Washington University, Aug. 1987.

8. Potter,A.E.Jr, Heimel,S., and Butler,J.N. : Apparent Flame Strength; A Measure of Maximum Reaction Rate in Diffusion Flames, Eighth (International) Symposium on Combustion, pp.1027-1034, 1962.

9. Tsuji,H., and Yamaoko,I. : The Counterflow Diffusion Flame in the Forward Stagnation Region of a Porous Cylinder, Eleventh (International) Symposium on Combustion, pp.979-984, 1967.

10. Tsuji,H., and Yamaoko,I. : The Structure of Counterflow Diffusion Flames in the Forward Stagnation Region of a Porous Cylinder, Twelfth (International) Symposium on Combustion, pp.997-1005, 1969.

11. Yamaoko,I., and Tsuji,H. : Determination on Burning Velocity using Counterflow Flames, Twentieth (International) Symposium on Combustion, pp.1883-1892, 1984.

12. Tsuji,H. : Counterflow Diffusion Flames, Prog. Energy Combust. Sci., pp.93-119, 1982.

13. Smooke,M.D., Puri,I.K., and Seshadri, K. : A Comparison Between Numerical Calculations and Experimental Measurements of the Structure of a Counterflow Diffusion Flame Burning Diluted Methane in Diluted Air, Twenty-First (International) Symposium on Combustion, pp.1783-1792, 1986.

14. Seshadri,K., Trevino,C., and Smooke,M.D. : Analysis of the Structure and Mechanisms of Extinction of a Counterflow Methanol-Air Diffusion Flame, Combustion and Flame, pp.111-132, 1989.

15. Pandya,T.P., and Weinberg,F.J. : The Structure of Flat, Counterflow Diffusion Flames, Proc. of the Royal Society, pp.544-561, 1964.

16. Peters,N., and Kee,R.J. : The Computation of Stretched Laminar Methane-Air Diffusion Flames Using a Reduced Four-Step Mechanism, Combustion and Flame, pp.17-29, 1987.

17. Kee,R.J., Miller,J.A., Evans,G.H., and Dixon-Lewis,G. : A Computational Model of the Structure and Extinction of Strained, Opposed Flow, Premixed Methane-Air Flames, Twenty-Second (International) Symposium on Combustion, 1988.

18. Bloor,M.I.G., David,T., Dixon-Lewis,G., and Gaskell,P.H. : The Influence of Combustion on the Fluid Structure in a Counterflow Diffusion Flame, Twenty-First (International) Symposium on Combustion, pp.1501-1509, 1986.

19. Chelliah,H.K.,Law,C.K.,Ueda,T.,Smooke,M.D., and Williams,F.A. : An Experimental and Theoretical Investigation of the Dilution, Pressure and Flow-field Effects on the Extinction Condition of Methane-Air-Nitrogen Diffusion Flames, Presented at Twenty-Third (International) Symposium on Combustion, 1990.

20. Spalding,D.B. : A Theory of Extinction of Diffusion Flames, Fuel, pp. 255-273, 1954.

21. Burke,S.P., and Schumann,T.E.W. : Diffusion Flames, Indust. Eng. Chem., pp.998-1004, 1928.

22. Spalding,D.B. : Theory of Mixing and Chemical Reaction in the Opposed-Jet Diffusion Flame, ARS Journal, pp.763-771, 1961.

23. Yeh,Y., and Cummins,H.Z. : Localized Flow Measurements With an He-Ne Laser Spectrometer, Appl. Phys. Letters 4, pp.176, 1964.

24. Rudd,M.J. : A New Theoretical Model For The Laser Dopplermeter, J. Phys. E. Sci.: Instrum. 2, pp.55, 1969.

25. Durst,F., Melling,A., and Whitelaw,J.H. : Principles and Practice of Laser-Doppler Anemometry, 2nd Ed., Academic Pres., New York, 1976.

26. TSI : Counter-Type Signal Processor Instruction Manual, 1985

27. Jarrett,O.Jr, Cutler,A.D., Antcliff,R.R., Chitsomboon,T., Dancey,C.L., and Wang,J.A. : Measurements of Temperature, Density, and Velocity in Supersonic Reacting Flow For CFD Code Validation, Presented at 25th JANNAF Combustion Meeting, Oct 1988.

28. Dancey,C.L. : Private Communication, 1990.

29. TSI : Frequency Shift System Instruction Manual, 1985.

30. Dancey,C.L. : Comparison of a Two Spot LTA System and a Three Color, Three Component LDA System When Measuring Turbulent Shear Flows, Report submitted to Universal Energy System, No F33615-84-C-2447, 1984.

31. Panton,R.L. : Incompressible Flow, John Wiley & Sons, New York, 1984.

32. Taylor,J.R. : An Introduction to Error Analysis, Oxford Uni. Pres., CA, 1982.

33. TSI : 3 Color, 3 Component Laser Doppler Velocimeter Instruction Manual, 1985.

34. Meyer,J.F., and Feller,W.V. : Wind Tunnel Measurements; LDV Characteristics, Proc. of First Int. Workshop on Laser Velocimetry, pp.445, 1972.

35. Hanson,S. : Visualization of Alignment Errors and Heterodyning Constraints in Laser Doppler Velocimeters, Proc. of LDA Symposium, pp.176-182, 1975.

36. Wang,J.C.F. : Measurement Accuracy of Flow Velocity via a Digital-Frequency-Counter Laser Velocimeter Processor, Proc. of LDA Symposium, pp.150-175,1975.

APPENDIX A

Error Propagation and LDA Uncertainty Analysis

The following are most of the possible sources of uncertainty that will contribute to the final uncertainty in the calculated velocities:[30]

- Fringe spacing uncertainty.
- Uncertainty in the angular orientation of the Blue and Green beams.
- Counter clock uncertainty due to the finite clock rate.
- Data word truncation uncertainty.
- Signal to Noise Ratio (SNR) effects.
- Angular bias error (for turbulent flows).
- Particle lag error.
- Statistical sampling error.
- Velocity bias error (for turbulent flows).

The LDA system used for the reported measurements has the following characteristics:

- 2 component fringe mode LDA (Ar^+ cw laser, 514.5 nm and 488.0 nm).
- ~0.5 watt laser power on both lines.
- 40 MHz Bragg shift on both channels, with downmixing.
- ~22° off-axis back scatter collection.
- Counter-based signal processing (with 1%, 5/8 comparison, 10 μsec coincidence).
- ~0.064 mm x ~0.15 mm measurement volume.[28]
- 7.3 μm (Blue) & 7.9 μm (Green) fringe spacing.

The measured velocity component by a LDA system is given as:

$$V = d_f \cdot f_D \tag{A1}$$

where d_f : fringe spacing
f_D : Doppler frequency

The uncertainty associated with the above velocity is found by taking the derivative of the above equation,

$$\Delta V = \frac{\partial V}{\partial d_f}\Delta d_f + \frac{\partial V}{\partial f_D}\Delta f_D$$

$$= f_D \Delta d_f + d_f \Delta f_D \qquad \text{(A2)}$$

Therefore, the uncertainty in the velocity V, by the rule of Sum in Quadrature[32] since Δd_f and Δf_D are independent variables is given by:

$$\frac{\Delta V}{V} = \sqrt{\left(\frac{\Delta d_f}{d_f}\right)^2 + \left(\frac{\Delta f_D}{f_D}\right)^2} \qquad \text{(A3)}$$

where ΔV is the uncertainty in the computed velocity
Δd_f is the uncertainty in the fringe spacing
and Δf_D is the uncertainty in the Doppler frequency

Fringe Spacing Uncertainty (Δd_f)

The uncertainty in fringe spacing measurement will show up as systematic error in the velocity uncertainty analysis.

The several sources of uncertainty in the determination of the fringe spacing are:

- uncertainty in beam-crossing angle (by and large, the largest source of error)
- uncertainty in laser wavelength λ_L(usually considered negligible)

- optical alignment error

The fringe spacing (d_f), is given by:[33]

$$d_f = \frac{\lambda_L}{2\sin\beta} \tag{A4}$$

where $\beta = \phi/2$ half angle between the two intersecting beams of each channel and λ_L is the wavelength of the two beams. Again using the sum in quadrature, estimation for the uncertainty in d_f yields:

$$\Delta d_f = \sqrt{\left(\frac{\partial d_f}{\partial \lambda_L}\right)^2 \Delta\lambda_L^2 + \left(\frac{\partial d_f}{\partial \beta}\right)^2 \Delta\beta^2}$$

$$= \sqrt{\left(\frac{\lambda_L}{2\sin\beta\tan\beta}\right)^2 \Delta\beta^2}$$

$$= \frac{\lambda_L}{2\sin\beta\tan\beta}\Delta\beta \tag{A5}$$

where it is assumed $\Delta\lambda_L = 0$.

Therefore, the relative fringe spacing uncertainty is,

$$\frac{\Delta d_f}{d_f} = \frac{\Delta\beta}{\tan\beta}\cdot 100\% \qquad \text{(A6)}$$

Measurement of the beam-crossing angle is done by the protractor method whereby the protractor's scale can be read to 1 minute of a degree. Therefore, there is some uncertainties associated with this finite scale of 1 minute. A set of five readings were made on the cross beam angle, to obtain an average reading and its standard deviation.

for the Blue line:

d_f = 7.281 µm
λ_L = 488 nm
$\phi/2$ = 115' ± 3'

Substituting, the blue line fringe spacing uncertainty is found to be $\frac{\Delta d_f}{d_f} = 2.61\%$.

For the Green line:

d_f = 7.907 µm
λ_L = 514.5 nm
$\phi/2$ = 112' ± 2'

and the green line fringe spacing uncertainty is $\frac{\Delta d_f}{d_f} = 1.79\%$

In addition to the uncertainty due to beam intersecting angle measurements, there is uncertainty in fringe spacing due to optical alignment caused by 1) the pair of beams not crossing at the waist of the Gaussian beams, and 2) the beams not aligned perpendicular to plane of the exit lens.

When the intersecting beams do not cross at their respective waists, a set of diverging fringes within the probe volume is generated. Thus, when particles pass through the probe volume perpendicular to the optical axis but at different positions, they will produce Doppler signals of different frequencies even though their velocities are identical. These differences in Doppler frequencies will show up as turbulence in the final data processing.

This alignment error is split into both fixed and random errors contributions. The fixed error will cause a bias in the fringe spacing, and is given as:[34]

$$\varepsilon_{bias} = \frac{D_{CV}-D_{BW}}{D_{CV}} \approx 0.01\% \qquad \text{(A7)}$$

where $D_{CV} = \sqrt{D_{BW}^2[1+(\frac{\lambda \Delta z}{\pi D_{BW}^2})^2]}$

and

D_{CV} = common-volume diameter
D_{BW} = beam waist diameter
Δz = distance between D_{CV} & D_{BW}

The random error contribution will show up as "artificial" turbulence, and is given by:

$$\frac{\Delta f_D}{f_D} = \frac{L_{CV}}{\Delta z\,[1+(\frac{\pi D_{CV}^2}{\lambda \Delta z})^2]} \tag{A8}$$

$$\approx 0.002\ \%$$

where L_{CV} is the common volume length, and Δz is estimated by magnifying and projecting the beams onto a wall, and measured the distance between D_{CV} and D_{BW} with the traverse table.

Another optical alignment error is present when the beams are not perpendicular to the plane of the exit lens. A set of parallel fringes with increasing fringe spacing perpendicular to the optical axis is generated.

This fringe broadening primarily has three important effects:

- Different Doppler signals are produced if particles in the same direction travel through the measurement volume at different locations within the probe volume.
- For a particle of constant velocity an increasing or decreasing Doppler frequency may be detected which could be mistaken as a velocity gradient. This error is partially reduced by the use of the counter comparison function.

- Different Doppler frequencies will be detected, if two particles having the same velocity magnitude but reverse direction, travel through the measurement volume.

Further treatments of these optical alignment errors can be found in Ref[35]. This optical alignment error will show as turbulent intensity in the final data processing.

Counter Clock Uncertainty (ε_D)

The signal counter used for these measurements has a 1 GHz clock speed to time the preselected 8 cycles of each Doppler burst. Since this clock uses a finite clock tick of 1 ns, for one burst measurement the uncertainty in timing that burst will be ±1 ns. This ±1 ns can be associated with two sources identified as synchronization and quantizing errors.[36]

Synchronization Error

The TSI counter will trigger the timer only after the signal has crossed the ±50 mV threshold level. The counter then counts zero-crossings and the number of clock ticks needed for eight such crossings. However, the first clock tick counted may not coincide with the first zero-crossing. This is termed the synchronization error.

Quantizing Error

This error is associated with the end part of each counted burst. After the 8 preselected zero-crossing, the counter will close the clock tick counting gate. But the 8th crossing may not coincide with the clock tick, thus introducing an error in the timing.

If these synchronization and quantizing errors within each measurement are repeated for 1024 measurements per sample, the relative error in the Doppler frequency detected can be approximated (for eight fringe crossings) by the following:[30]

$$\varepsilon_D(\%) = 7.22\left(\frac{f_D}{f_C}\right)\left(1+\frac{f_S}{f_D}\right)^2 \tag{A9}$$

where f_D = Doppler frequency
f_C = counter clock frequency (1GHz)
f_S = shift frequency (500kHz, preset)

Note, however, that this error is a function of f_D only, since f_S & f_C are kept fixed in the present reported experiment. For example, for a measured velocity of V=100cm/s, the ε_D is ~0.02%. The counter clock error, ε_D, is essentially a random error in the velocity uncertainty, since f_D is proportional to V.

Data Truncation Error (ε_{Db})

The TSI counter uses a 24 bit data word for the clock tick counting, but this word is put into a 16 bit data word (b) for the computer interface. The relative error in the

Doppler frequency associated with this truncation process of the Doppler frequency data word is estimated as:[30]

$$\varepsilon_{Db} = 2^{-b}(1+\frac{f_S}{f_D})\cdot 100\% \qquad \text{(A10)}$$

Note that this error is inversely proportional to the Doppler frequency (f_D), for example, for V=10 cm/s ε_{Db} is ~0.003%. Again, note that this error is part of the random error inherent in this experimental measurements.

Signal to Noise Ratio (SNR)

It is found that the uncertainty in a measurement increases as the SNR decreases,[30] and this type of error is not expected to be serious for mean velocity measurements. SNR has not been satisfactorily quantified. The followings are sources which can give rise to noise effects:

- light scattering off the equipment (in this case: burner box, which is made of polycarbonate plastics; the aluminum tube holder; internal reflections off the optical system; etc)

- electronics (PMT amplifier; counter conditioner amplifier; etc)

This type of error can be reduced by narrow band pass filterings.

Statistical Bias

Statistical bias is due to the fact that the true value was derived from a finite (1024) measurements. This error bias is estimated using the standard error of the mean:[32]

$$\sigma_{\bar{x}} = \frac{\sigma_x}{\sqrt{N}} \tag{A14}$$

where σ_x is the standard deviation, and N is the number of measurements

For example, a measured velocity of V=100cm/s has a deviation of σ_x=3cm/s ∴ error due to 1024 measurements is ~0.09%.

In summary, the uncertainties in the measured velocities consist of both the fixed and the random errors. From the above analysis, the fixed error for this experiment is estimated to be ~2.7% for the blue line, and ~1.8% for the green line, with the largest contribution from fringe spacing uncertainty. The random error is estimated to be ~0.9%. However, burner equipment (eg. gas regulator, valves, etc) also contributed to a random error. It is estimated that the velocity uncertainty including random error is ~3%. The particle lag error is more difficult to estimate with confidence, but based upon modeling results and observed measurements, it is estimated to be ~3-5%.

APPENDIX B. Experimental Data

Table 1 Experimental data at the lower strain rate case

Axial *z* mm	Radial *r* mm	Axial *u* cm/s	Radial *v* cm/s	Axial *z* mm	Radial *r* mm	Axial *u* cm/s	Radial *v* cm/s
0.00	-0.40	72.46	2.47	3.50	2.00	37.11	36.48
0.00	-0.30	72.81	2.65	3.50	2.50	36.18	43.85
0.00	-0.20	73.06	2.76	3.50	3.00	35.15	48.61
0.00	-0.10	73.08	2.99	3.50	3.50	24.23	48.80
0.00	0.00	73.14	3.03	3.50	4.00	24.90	48.66
0.00	0.50	71.49	3.67	3.50	4.50	27.45	45.71
0.00	1.00	67.43	4.21	4.00	0.00	62.00	1.26
0.00	1.50	60.07	4.73	4.00	0.50	61.11	12.43
0.00	2.00	50.42	4.68	4.00	1.00	59.73	23.05
0.00	2.50	37.44	4.17	4.00	1.50	58.11	33.25
0.00	3.00	21.30	3.22	4.00	2.00	59.18	43.57
2.50	0.00	50.33	1.94	4.00	2.50	57.04	50.69
2.50	0.50	48.96	6.41	4.00	3.00	50.89	55.38
2.50	1.00	46.06	10.84	4.00	3.50	49.02	57.01
2.50	1.50	41.44	14.83	4.00	4.00	48.86	55.59
2.50	2.00	35.23	18.35	4.00	4.50	48.58	52.20
2.50	2.50	27.76	20.34	4.50	0.00	93.59	1.89
2.50	3.00	18.25	22.44	4.50	0.50	92.46	15.47
2.50	3.50	9.71	23.15	4.50	1.00	90.54	27.80
2.50	4.00	3.74	24.32	4.50	1.50	87.60	39.70
3.00	0.00	40.66	1.41	4.50	2.00	82.86	48.94
3.00	0.50	39.31	7.20	4.50	2.50	77.46	56.26
3.00	1.00	36.43	13.11	4.50	3.00	72.68	59.79
3.00	1.50	32.49	18.17	4.50	3.50	68.56	60.84
3.00	2.00	26.97	22.82	4.50	4.00	64.70	59.63
3.00	2.50	20.32	28.02	4.50	4.50	61.96	56.35
3.00	3.00	14.01	32.41	5.00	0.00	102.54	3.43
3.00	3.50	10.49	36.46	5.00	0.50	99.87	17.14
3.00	4.00	8.69	37.14	5.00	1.00	96.34	29.88
3.00	4.50	10.39	34.95	5.00	1.50	91.39	41.73
3.50	0.00	40.92	0.46	5.00	2.00	86.60	51.11
3.50	0.50	39.92	9.69	5.00	2.50	81.67	58.22
3.50	1.00	39.20	18.80	5.00	3.00	78.29	63.31
3.50	1.50	38.44	27.86	5.00	3.50	73.76	64.74

Table 1 Con't

Axial *z* mm	Radial *r* mm	Axial *u* cm/s	Radial *v* cm/s	Axial *z* mm	Radial *r* mm	Axial *u* cm/s	Radial *v* cm/s
5.00	4.00	70.43	63.68	0.20	0.00	73.41	3.28
5.00	4.50	68.02	60.16	0.40	0.00	72.54	3.28
5.50	0.00	86.61	1.49	0.60	0.00	71.55	3.19
5.50	0.50	83.47	16.58	0.80	0.00	70.44	3.32
5.50	1.00	79.77	29.88	1.00	0.00	69.10	3.19
5.50	1.50	76.41	42.82	1.20	0.00	67.74	2.99
5.50	2.00	75.96	54.07	1.40	0.00	65.76	2.73
5.50	2.50	72.22	61.96	1.60	0.00	63.90	2.59
5.50	3.00	69.52	67.65	1.80	0.00	61.72	2.49
5.50	3.50	68.95	69.02	2.00	0.00	59.11	2.46
5.50	4.00	68.02	67.66	2.20	0.00	56.08	2.48
5.50	4.50	67.65	63.91	2.40	0.00	49.68	2.20
6.00	0.00	57.87	-2.48	2.60	0.00	46.34	1.78
6.00	0.50	54.72	14.79	2.80	0.00	41.92	1.52
6.00	1.00	52.01	29.99	3.00	0.00	37.50	1.16
6.00	1.50	49.14	44.55	3.20	0.00	35.05	0.93
6.00	2.00	48.54	57.08	3.40	0.00	32.10	0.58
6.00	2.50	49.08	66.68	3.60	0.00	37.31	0.54
6.00	3.00	50.43	72.97	3.80	0.00	50.43	0.83
6.00	3.50	54.46	75.79	4.00	0.00	69.10	1.85
6.00	4.00	59.24	74.27	4.20	0.00	81.59	1.95
6.00	4.50	62.23	70.43	4.40	0.00	95.03	1.85
6.50	0.00	16.83	-6.80	4.60	0.00	101.58	1.74
6.50	0.50	12.62	11.33	4.80	0.00	104.20	2.75
6.50	1.00	9.73	29.73	5.00	0.00	103.76	3.17
6.50	1.50	17.20	46.81	5.20	0.00	98.72	2.66
6.50	2.00	23.58	62.45	5.40	0.00	89.59	2.03
6.50	2.50	25.23	72.68	5.60	0.00	77.73	1.24
6.50	3.50	37.51	82.32	5.80	0.00	64.31	0.31
6.50	4.00	43.85	83.10	6.00	0.00	48.30	-0.87
6.50	4.50	53.02	78.71	6.20	0.00	33.08	-2.23
0.00	0.00	74.05	3.08	6.40	0.00	18.37	-3.47

Table 2 Experimental data at the higher strain rate case

Axial z mm	Radial r mm	Axial u cm/s	Radial v cm/s	Axial z mm	Radial r mm	Axial u cm/s	Radial v cm/s
0.00	-0.40	94.43	2.81	3.00	0.00	50.79	1.18
0.00	-0.30	95.23	2.86	3.00	0.50	50.06	9.78
0.00	-0.20	95.56	3.11	3.00	1.00	47.50	18.50
0.00	-0.10	95.83	3.53	3.00	1.50	43.57	25.73
0.00	0.00	95.90	3.44	3.00	2.00	46.22	27.11
0.00	0.50	94.69	4.16	3.00	2.50	39.64	29.34
0.00	1.00	89.81	5.10	3.00	3.00	27.59	35.04
0.00	1.50	81.11	5.52	3.00	3.50	15.21	41.27
0.00	2.00	68.99	5.64	3.00	4.00	8.02	43.01
0.00	2.50	52.43	4.92	3.00	4.50	4.08	42.78
0.00	3.00	32.50	3.81	3.50	0.00	37.88	0.24
0.00	3.30	17.23	2.42	3.50	0.50	37.61	11.75
2.00	0.00	76.95	2.31	3.50	1.00	35.19	22.59
2.00	0.50	76.08	7.02	3.50	1.50	32.66	33.98
2.00	1.00	72.96	11.29	3.50	2.00	30.45	44.20
2.00	1.50	67.30	14.84	3.50	2.50	27.05	53.37
2.00	2.00	59.03	17.06	3.50	3.00	23.97	60.73
2.00	2.50	47.91	18.17	3.50	3.50	20.84	65.48
2.00	3.00	34.13	16.99	3.50	4.00	17.81	67.08
2.00	3.50	20.48	13.88	3.50	4.50	16.42	64.64
2.50	0.00	66.47	2.02	4.00	0.00	84.57	0.02
2.50	0.50	65.20	8.30	4.00	0.50	81.74	18.11
2.50	1.00	67.49	12.93	4.00	1.00	77.42	35.25
2.50	1.50	64.29	16.42	4.00	1.50	73.78	50.16
2.50	2.00	53.46	21.65	4.00	2.00	46.94	54.35
2.50	2.50	42.18	26.26	4.00	2.50	44.54	65.30
2.50	3.00	31.25	27.02	4.00	3.00	52.25	79.62
2.50	3.50	19.86	25.21	4.00	3.50	49.36	84.58
2.50	4.00	10.81	22.79	4.00	4.00	45.42	84.54
2.50	4.50	4.39	20.18	4.00	4.50	40.75	80.09

Table 2 Con't

Axial *z* mm	Radial *r* mm	Axial *u* cm/s	Radial *v* cm/s	Axial *z* mm	Radial *r* mm	Axial *u* cm/s	Radial *v* cm/s
4.50	0.00	103.98	-1.25	5.50	4.50	71.01	99.16
4.50	0.50	102.57	21.88	0.00	0.00	96.20	3.58
4.50	1.00	99.62	43.95	0.20	0.00	95.47	3.63
4.50	1.50	94.13	59.51	0.40	0.00	94.57	3.39
4.50	2.00	86.69	72.34	0.60	0.00	93.85	3.27
4.50	2.50	80.90	83.80	0.80	0.00	92.46	3.58
4.50	3.00	76.93	91.72	1.00	0.00	92.75	3.78
4.50	3.50	70.32	94.89	1.20	0.00	91.79	3.48
4.50	4.00	66.87	95.11	1.40	0.00	89.55	3.04
4.50	4.50	63.47	90.75	1.60	0.00	85.85	2.80
5.00	0.00	66.96	-3.24	1.80	0.00	81.16	2.65
5.00	0.50	64.71	25.18	2.00	0.00	78.55	2.67
5.00	1.00	63.07	50.19	2.20	0.00	74.40	2.43
5.00	1.50	67.00	72.32	2.40	0.00	69.20	2.39
5.00	2.00	68.87	89.23	2.60	0.00	65.60	1.94
5.00	2.50	70.92	105.02	2.80	0.00	58.76	1.64
5.00	3.00	72.81	111.40	3.00	0.00	52.86	1.41
5.00	3.50	73.77	113.45	3.20	0.00	46.30	1.02
5.00	4.00	74.80	110.15	3.40	0.00	39.24	0.51
5.00	4.50	75.44	102.76	3.60	0.00	39.20	-0.08
5.50	0.00	4.18	-4.53	3.80	0.00	38.54	0.23
5.50	0.50	3.26	23.39	4.00	0.00	46.27	0.03
5.50	1.00	5.79	51.74	4.20	0.00	69.27	-0.45
5.50	1.50	11.56	77.05	4.40	0.00	98.18	-1.04
5.50	2.00	21.84	98.98	4.60	0.00	104.52	-0.87
5.50	2.50	32.10	115.54	4.80	0.00	97.11	-0.97
5.50	3.00	44.57	124.60	5.00	0.00	81.04	-1.66
5.50	3.50	56.63	128.17	5.20	0.00	56.95	-2.38
5.50	4.00	66.38	124.13	5.40	0.00	37.03	-3.34

VITA

Siew-Hock Yeo, the seventh child of Mr & Mrs Yeo Boon Hiong, was born on May 30, 1963 in Singapore. He began his life in Mechanical Engineering by attending Ngee Ann Polytechnic in 1980. He then attended Florida Institute of Technology in 1985, and graduated with a Bachelor of Science in Mechanical Engineering in 1988. He continues his life in Mechanical Engineering at Virginia Tech as a graduate student.

Yeo Siew Hock.

Siew-Hock Yeo